People's Democratic Republic Of Algeria

وزارة التـــــعـــليـــم العـــــــــــالي والبـــــــحث العـــــــــلـــمـــــي

Ministry of Higher Education and Scientific Research

جـــــــــــــــــــــــــــامعة سعيدة – د. الطاهر مولاي–

University Of Saïda -Dr Moulay Tahar
Technology Faculty

Department of Process Engineering

END-OF-CYCLE PROJECT

Submitted for the Master's Degree in Process Engineering

Major :Material Process Engineering

Local Production of a Dental Ceramic Coating

Presented by:

Acid Omar Elfarouk **Fettouh Hocine**

Supervised , on 01/12/2025 , in front of jury composed of :

Dr A. Benhlima	**President**
Dr O. Belarbi	**Supervisor**
Pr M. Adjdir	**Co .Supervisor**
Dr M. Boudinar	**Examiner**

Academic year 2024/2025

Abstract

New bioactive materials for dental ceramic coatings were developed from an industrial residue, carbide lime, a by-product of acetylene production predominantly composed of calcium hydroxide. After purification and sulfur removal, this waste was converted into hydroxyapatite powders by a wet-chemical precipitation method, using different particle-size fractions of the carbide lime to tailor the crystallinity and morphology of the synthesized hydroxyapatite. These powders were then used as precursors for zinc-doped hydroxyapatite obtained via a mechanochemical route, yielding materials with controlled particle size and preserved apatite structure. The zinc-modified hydroxyapatites exhibited measurable antibacterial activity against oral bacteria, with inhibition zones between 9 and 25 mm depending on particle size, zinc precursor and bacterial strain, while the ZnA-45Hap composition showed the most balanced behavior, combining limited antibacterial effect with good compatibility for oral applications. This approach demonstrates the feasibility of valorizing local industrial waste into functional bioceramic materials for future dental coating applications.

Key words: carbide lime, hydroxyapatite, zinc-doped hydroxyapatite, antibacterial, dental coatings, biomaterials, waste valorization.

ملخص

تم تطوير مواد حيوية جديدة فعّالة حيوياً لاستخدامها كطبقات خزفية للأسنان انطلاقاً من راسب صناعي هو كربيد الكالسيوم، وهو ناتج ثانوي لعملية إنتاج الأسيتيلين ويتكوّن أساساً من هيدروكسيد الكالسيوم. بعد التنقية وإزالة الكبريت، حُوِّلت هذه النفاية إلى مساحيق من هيدروكسي أباتيت باستعمال طريقة الترسيب الكيميائي الرطب، مع استخدام كسور مختلفة من أحجام حبيبات كربيد الكالسيوم لضبط درجة التبلور والمورفولوجيا لهيدروكسي الأباتيت المُحضَّر. استُخدمت هذه المساحيق لاحقاً كمادة أولية لتحضير هيدروكسي أباتيت مطعَّم بالزنك عبر مسار ميكانيكي-كيميائي، مما أتاح الحصول على مواد ذات حجم حبيبي مضبوط مع الحفاظ على البنية الأباتيتية. أظهرت عينات هيدروكسي الأباتيت المطعَّمة بالزنك نشاطاً مضاداً للبكتيريا يمكن قياسه ضد البكتيريا الفموية، مع مناطق تثبيط تراوحت بين 9 و25 مم تبعاً لحجم الحبيبات ونوع سلف الزنك والسلالة البكتيرية، في حين قدّمت تركيبة ZnA-45Hap سلوكاً أكثر توازناً من خلال الجمع بين تأثير مضاد للجراثيم محدود وتوافقية جيدة مع الوسط الفموي. تبرهن هذه المقاربة على إمكانية تثمين النفايات الصناعية المحلية وتحويلها إلى مواد بيوخزفية وظيفية مهيأة لتطبيقات الطلاءات الخزفية السنية المستقبلية.

الكلمات المفتاحية: كربيد الكالسيوم، هيدروكسي أباتيت، هيدروكسي أباتيت مطعَّم بالزنك، مضاد للبكتيريا، طلاءات سنية، مواد حيوية، تثمين النفايات.

Dedication

I dedicate this modest work:

To my dear parents, whose unwavering support, patience, and encouragement have guided me through every stage of my academic journey.

To my beloved mother, whose boundless love and countless sacrifices can never be captured in words. May God protect you and bless you with health, happiness, and a long life.

To my dear brother, Fethi, whose presence, motivation, and steadfast belief in me have strengthened me and contributed to every success I have achieved.

To my fellow classmates and colleagues, who have shared with me both the challenges and the triumphs of this academic path. Your collective energy, creativity, and dedication have created an environment that has inspired me to learn, grow, and persevere.

I also wish to thank my binôme, Hocine, for his support, cooperation, and valuable contribution to this work.

I would also like to express my deep gratitude to Aounallah, whose valuable assistance and provision of essential tools greatly facilitated the preparation and accomplishment of this project.

Omar Elfarouk

Dedication

I would like to express my deepest gratitude to my beloved parents, whose support, prayers, and sacrifices have been the foundation of my success. Every step I have achieved was made possible through their constant encouragement and unconditional love. My heartfelt thanks also go to my siblings and to my brother's wife for their continuous support.

My sincere appreciation goes to my esteemed professor for her invaluable guidance, knowledge, and dedication throughout my academic journey.

I wish to extend my thanks to my cousin for his valuable assistance during my internship in the Wilaya of Sidi Bel Abbès.

A special thank-you goes to my binôme, Omar Elfarouk, for his collaboration, support, and companionship throughout this work.

Finally, I express my gratitude to all my university colleagues for their support, especially Settouti**.**

Hocine

Acknowledgements

Above all, we express our profound gratitude to **Allah, the Most Merciful**, for granting us the strength, perseverance, and clarity of mind needed to undertake and complete this modest work.

We extend our heartfelt thanks to **Mrs. O. Belarbi**, whose scientific guidance and constant support greatly enriched this study. Her dedication, availability, and rigorous supervision were essential at every stage of this project, and we are sincerely grateful for her invaluable contribution.

Our deep appreciation goes to **Mr. M. Adjdir** for his insightful suggestions, scientific input, and collaboration, which helped shape the synthesis strategy and strengthen the outcomes of this work.

We would also like to express our sincere gratitude to **Dr. A. Benhlima**, President of the jury, and **Dr. M. Boudinar**, Examiner, for honoring us with their presence, carefully evaluating our work, and providing constructive comments that have enriched the scientific quality of this study.

We extend our warm thanks to **Mr. M. Bellayachi** and to **Linde Gas in Sidi Bel Abbès** for their assistance and support during our internship, which greatly helped us in the accomplishment of this thesis.

We are equally grateful to **Mr. M. Alaam**, Head of Research and Development at **ABRA-Saida**, for granting us access to the company's facilities and providing the necessary conditions to carry out our experimental work.

We would also like to thank the **responsible staff of LTPO** for their technical assistance and for providing optimal working conditions and essential equipment, which greatly facilitated and accelerated our experimental procedures.

Our gratitude extends to **Mr. A. Ammam** and **Mrs. H. Belgacem** for their contributions to the microbiological aspect of this study, including antimicrobial testing, culture media preparation, and biological assays.

We would also like to express our sincere appreciation to **Mrs. Soufal**, thanks to whom we were able to carry out the analyses in Sidi Bel Abbès. Her help was essential to the progress of this work.

We also extend our thanks to **Mr. Daoudi** for his valuable contribution to the IRTF analyses, which significantly enriched the analytical part of our study.

We would also like to warmly thank **Mrs. S. Lahreche and Z. Jellouli**, the laboratory responsables at our university, for their valuable assistance, support, and guidance throughout our practical work.

We are also thankful to the **Process Engineering Department**, whose members supported us throughout our academic journey and contributed significantly to the completion of this work.

Finally, we express our sincere appreciation to all those who, directly or indirectly, helped, encouraged, or advised us. Each gesture of support contributed to bringing this work to fruition.

Table of Contents

List of abbreviations

EPS	Extracellular polymeric substances
pH	potential of Hydrogen
FTIR	Fourier-Transform Infrared Spectroscopy
EDS	Energy Dispersive X-ray Spectroscopy
XRD	X-Ray Diffraction
LTPO	Laboratoire des Travaux Publics de l'Ouest
LOI	Loss of Ignition
XRF	X-ray fluorescence
IR	Infrared Spectroscopy
Hap	Hydroxyapatite

List of Figures

List of Tables :

General Introduction

General Introduction :

In recent years, biomaterials have gained growing importance in the fields of medicine and dentistry due to their potential to restore lost or damaged tissues while ensuring long-term safety and functionality (Ratner et al., 2013). Biomaterial is any substance or a combination of substances that has been engineered to interact with biological systems. It can be either synthetic or natural in origin. It can partially or fully replace any body's tissues, organs, or function. Ceramics fall under the biomaterial class, i.e., they are mainly used as implant material in the biomedical engineering field (dos Santos, Chevalier, Fredel, Henriques, & Gremillard, 2024). Ceramics possess various good biocompatibility, excellent osteoconduction, and bioactivity (Youness, Al-Ashkar, & Taha, 2023). Among them, hydroxyapatite (HA) stands out because of its chemical and structural similarity to the mineral components of bone and teeth (Dorozhkin, 2010). However, pure HA presents certain limitations, such as low antibacterial activity and limited mechanical performance, which may compromise its clinical effectiveness, especially in dental applications (Hench & Wilson, 2013). To address these challenges, researchers have explored ionic doping, notably with zinc ions (Zn^{2+}), to enhance the biological, mechanical, and antibacterial properties of HA (Xiao et al., 2017). At the same time, there is an increasing need to develop sustainable synthesis methods that promote circular economy principles (García et al., 2020). A key obstacle of Hap synthesis as an biomaterial ceramics is the high synthesis cost. Commercial synthesis of HAp and its composites requires a large amount of chemicals, which can be both economically and environmentally taxing (Ali, Alrowaili, El-Giar, Ahmed , & El-Kady, 2021).

In this context, our project focuses on the transformation of an unused by-product from the industrial gas sector into a bioactive and antimicrobial coating material for dental ceramics. It is an industrial waste generated during acetylene production, called ‘carbide lime’ waste as a potential calcium source for the synthesis of HAp. Carbide lime is mainly composed of $Ca(OH)_2$ and can be used as a calcium source without any pre-treatment or energy-intensive calcination (Gong, et al., 2022). This is the primary objective of our work. In other wise, by enriching hydroxyapatite with zinc and sourcing calcium from hydrated lime waste, we aim to reduce production costs and improve clinical performance (Kumar et al., 2019). While Algeria currently relies entirely on imports for dental bioceramics, our local solution offers a strategic opportunity to achieve industrial sovereignty in a growing and vital healthcare sector. Our goal is to synthesize and characterize zinc-doped hydroxyapatite obtained from industrial waste and evaluate its physicochemical and antibacterial properties for dental applications. The material

is synthesized using a wet chemical precipitation method, followed by mechanochemical doping with zinc and thermal treatment (Chen et al., 2015). We employ techniques such as X-ray diffraction (XRD), Fourier-transform infrared spectroscopy (FTIR), particle size distribution, pH and conductivity measurement, and agar well diffusion to assess its structural and biological properties (Singh et al., 2018).

This study forms part of our startup's ongoing efforts to develop innovative, affordable, and locally produced bioceramic coatings tailored for applications in the Algerian dental sector

The present manuscript is organized into four chapters. The first chapter outlines a detailed review of the relevant literature. The second chapter details the experimental protocols and analytical techniques used. The third chapter deals with the physicochemical characterization of the waste materials used as precursors. The fourth chapter presents the experimental results related to the synthesis of the zinc-doped hydroxyapatite. Finally, a general conclusion highlights the main outcomes and proposes directions for future research.

General Introduction

References :

Ali, A. F., Alrowaili, Z. A., El-Giar, E. M., Ahmed, M. M., & El-Kady, A. M. (2021). Novel green synthesis of hydroxyapatite uniform nanorods via microwave-hydrothermal route using licorice root extract as template. *Ceramics International*, *47*(3), 3928–3933.

dos Santos, V., Chevalier, J., Fredel, M. C., Henriques, B., & Gremillard, L. (2024). Ceramics and ceramic composites for biomedical engineering applications via Direct Ink Writing: Overall scenario, advances in the improvement of mechanical and biological properties and innovations. *Materials Science and Engineering: R: Reports*, *161*(1).

Gong, X., Zhang, T., Zhang, J., Wang, Z., Liu, J., Cao, J., & Wang, C. (2022). Recycling and utilization of calcium carbide slag: current status and new opportunities. *Renewable and Sustainable Energy Reviews*, *159*, 112133.

Youness, R. A., Al-Ashkar, E., & Taha, M. A. (2023). Role of porosity in the strength, dielectric properties, and bioactivity of hardystonite ceramic material for use in bone tissue engineering applications. *Ceramics International*, *49*(24), 40520–40531.

Ratner, B. D., Hoffman, A. S., Schoen, F. J., & Lemons, J. E. (2013). *Biomaterials Science: An Introduction to Materials in Medicine*. Academic Press.

Dorozhkin, S. V. (2010). Bioceramics of calcium orthophosphates. *Biomaterials*, *31*(7), 1465–1485.

Hench, L. L., & Wilson, J. (2013). *An Introduction to Bioceramics*. World Scientific.

Xiao, W., et al. (2017). Zinc-doped hydroxyapatite: synthesis, characterization, and antibacterial properties. *Journal of Biomedical Materials Research Part A*, 105(4), 1097-1106.

García, M., et al. (2020). Circular economy approaches in biomaterials synthesis from industrial waste. *Sustainable Materials and Technologies*, 25, e00185.

Kumar, S., et al. (2019). Utilization of industrial lime waste for hydroxyapatite synthesis: A sustainable approach. *Journal of Cleaner Production*, 210, 1234-1242.

Chen, Y., et al. (2015). Mechanochemical synthesis of zinc-doped hydroxyapatite for biomedical applications. *Materials Science and Engineering: C*, 48, 1-7.

Singh, R., et al. (2018). Characterization and antibacterial evaluation of zinc-substituted hydroxyapatite. *Ceramics International*, 44(16), 19780-19789.

Chapter I :
Literature review

Chapter I : Literature review

1. General overview of Biomaterials :

The term “biomaterial” is often used to refer to a wide range of materials intended for biomedical applications (Sáenz et al., n.d.). Among these, calcium-based compounds, such as carbonates and phosphates, have emerged as prominent candidates. It can be largely attributed to the fact that natural bone is primarily composed of calcium phosphates, with hydroxyapatite (HA) receiving particular scientific interest due to its structural similarity to bone mineral and its biocompatibility (Quillard et al., 2011). Biocompatibility in this context denotes not only the absence of cytotoxic effects but also the capacity of the material to maintain chemical integrity and structural stability in physiological environments (Williams, 2008).

Recent advances in material science and processing technologies have enabled the development of ceramic materials with optimized physical, mechanical, and chemical properties, making them highly suitable for applications in both orthopedic and dental implants. Hydroxyapatite, being chemically similar to the mineral component of natural bone and enamel ($Ca_{10}(PO_4)_6(OH)_2$), demonstrates exceptional biocompatibility, which makes it particularly suitable for a range of dental applications such as bone grafts, dental implants, and coatings on titanium screws (Schmalz & Arenholt-Bindslev, 2009). In dentistry biomaterials play a key role in restoring function, aesthetics and structural integrity to damaged or lost dental tissue (Anusavice, 2012). They are used in various applications including implants, crowns, bridges, fillings and orthodontic devices (Sakaguchi, 2012).The choice of biomaterial depends on factors such as biocompatibility, mechanical properties and long term stability in the oral environment (Misch, 2007).

2. Classification of Biomaterials :

Biomaterials are categorized into four primary classes, each with distinct characteristics as it is illustrated in table I-1.

Among the four main categories of biomaterials, ceramics stand out for their unique combination of mechanical strength and biocompatibility

Table I-1: Classification of biomaterials based on composition and dental uses (Abraham & Venkatesan, 2022)

Class	Key Examples	Properties	Dental Applications
Metals	Titanium alloys, Stainless steel	High strength, ductility	*Implant fixtures, orthodontic wires*
Ceramics	Zirconia, Hydroxyapatite	Biocompatibility, aesthetics, wear resistance	*Crowns, implants, coatings*
Polymers	Acrylics, Silicone	Flexibility, ease of manipulation	*Dentures, impression materials*
Composites	Polymer-ceramic hybrids	Tailored strength and aesthetics	*Fillings, restorative materials*

3. Ceramic biomaterials :

Bioceramics refer to a class of biomaterials derived from the sintering or melting of inorganic raw materials to form amorphous or crystalline solid structures suitable for biomedical applications. These materials are primarily used as rigid components in surgical implants due to their mechanical strength and biocompatibility, although certain formulations can exhibit some degree of flexibility (dos Santos et al., 2024). Bioceramics are specifically engineered for the repair, reconstruction, or replacement of diseased or damaged tissues, particularly within the musculoskeletal system, including bone and dental structures (Prasad Kumara et al., 2025). There are three main classes of bioceramics.

3. 1 - Nonabsorbable (or Bioinert) Bioceramics:

These materials do not undergo significant degradation or chemical change upon implantation. As example Zirconia which is often used in dental technology, in form of pins, crowns (Figure **I-1**), implant abutments, bridges, veneers and orthodontic brackets (Della Bona et al., 2015)

Figure I-2:Zirconia full-coverage crown in dental applications (Agustín-Panadero et al., 2014)

3. 2 - Bioactive (or Surface-Reactive) Ceramics:

These ceramics are materials that interact with surrounding tissues by forming a biologically active layer on their surface. A key example is hydroxyapatite (HA) , used in dental implants (Figure I-3), bone grafting, and as a coating material to enhance integration with surrounding tissues (Gupta et al., 2025).

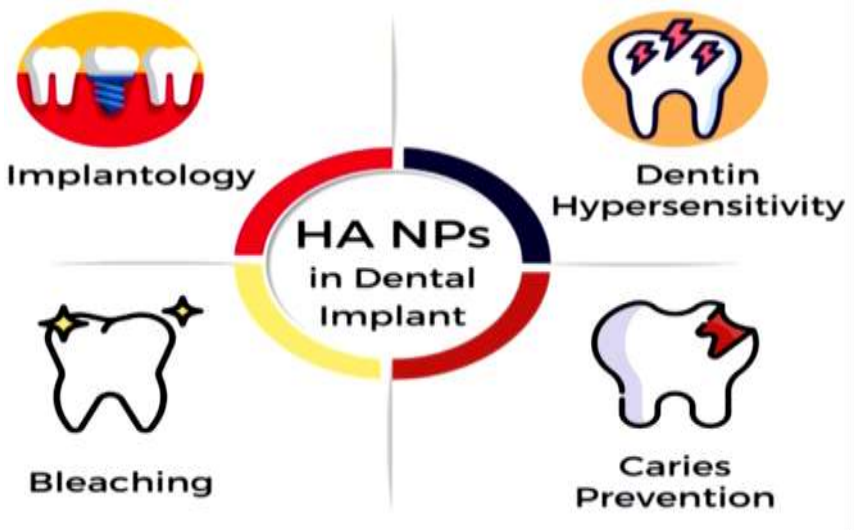

Figure I-4:HA in dental implants (Islam et al., 2025)

3. 3 - Biodegradable (or bioresorbable) ceramics:

There are designed to degrade progressively within the body after implantation as Tricalcium Phosphate. The figure I-5 illustrates some tricalcium phosphate applications in dentistry.

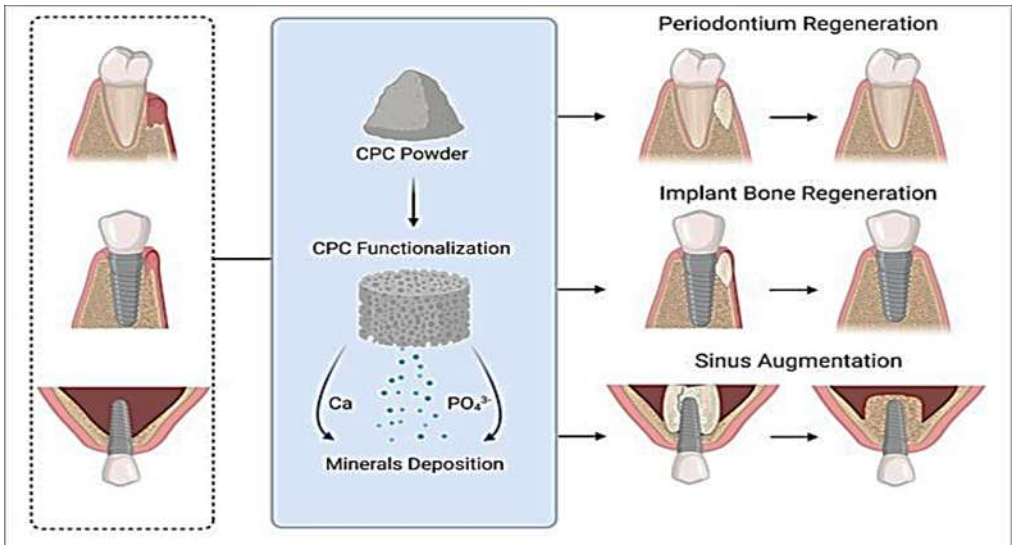

Figure I-6: some calcium phosphate compounds applications in dentistry *(Alsahafi et al., 2021)*

A particularly important subset of ceramic biomaterials is apatite-based ceramics, which closely mimic the mineral phase of bone and teeth.

4. Apatite based ceramics:

Apatite is a group of crystalline compounds ranging from natural apatite (minerals) to biological (human dentin, enamel, and bone) and synthetic (chemically synthesized) apatite (LeGeros, 1998) . The most common of these compounds is calcium hydroxyapatite. All the related crystal structures, such as fluorapatite, chlorapatite, and carbonate apatite, are derived from it.

Among apatite-based ceramics, hydroxyapatite is the most widely studied and applied, meriting focused attention due to its remarkable clinical potential.

5. Hydroxyapatite (Hap) :

Hydroxyapatite is the main inorganic constituent of the bone and tooth mineral (Tsetsekou et al., 2014; Yelten-Yilmaz & Yilmaz, 2018). Synthetic Hap is a bioceramic, which is stable from chemical, physiological and mechanical standpoints when it is in contact with the biological fluids (Gopi et al., 2012). In fact, it is a good candidate for bone substitute due to its biocompatibility, bioactivity, osteoconductivity, osteoinductivity, bone remodeling and bone formation capabilities, slow biodegradability, nontoxicity, non-inflammatory and long-term stability (Gopi et al., 2011). It can also be used for dental and bulk implant material, implant

coating, drug delivery systems and orthopedic applications for repairing or substituting hard tissues (Szcześ et al., 2017).

Hydroxyapatite with the chemical formula $Ca_{10}(PO)_6(OH)_2$, has the hexagonal $P6_3/m$ space group (Figure **I-7**).

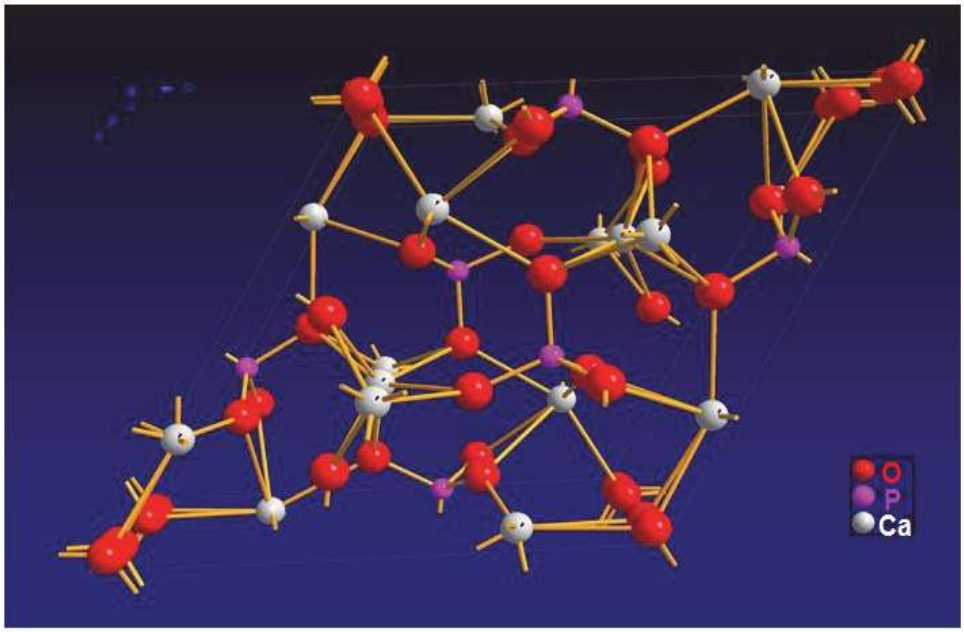

Figure I-8 :Crystal Structure of Hydroxyapatite (Rivera-Muñoz, 2011)

According to (LeGeros, 1998) the lattice parameters of mineralogical hydroxyapatite (found in Holly Springs, MS) are **a = 9.822 Å, c = 6.880 Å ± 0.003 Å**.

The crystal contains two types of Ca atoms: Ca I (4 atoms) at z = 0 and z = 1/2, and Ca II (6 atoms) forming a channel structure along the c-axis, creating a triangular arrangement around hydroxyl groups (Kandori et al., 2010);(Kandori et al., 2014);(Franzén et al., 2008).

5.1 Ionic Substitution in Hydroxyapatite :

The Hap lattice allows the incorporation of a wide array of substituent ions, influencing both structural and functional properties:

- Ca^{2+} substitution: Mg^{2+}, Ba^{2+}, Pb^{2+} (Bystrov et al., 2023; Vasant, 2024; J. Wang, 2015)
- $(PO_4)^{3-}$ substitution: $(BO_3)^{3-}$, vanadate, manganate, $(CO_3)^{2-}$, $(SiO_4)^{4-}$ (Deymier et al., 2017; H. Li et al., 2014; Suetsugu et al., 1998a)
- (OH^-) substitution: F^-, Cl^-, $(CO_3)^{2-}$ (Madupalli et al., 2017; Piccoli & Candela, 2002; Suetsugu et al., 1998a)

5.2 Effects on Lattice Parameters :

Fluorapatite, chlorapatite, and carbonate apatite are structurally derived from hydroxyapatite and exhibit modified lattice parameters (Elliott, 1994):

- Fluorapatite (F^- substitution): a = 9.382 Å, c = 6.880 Å
- Chlorapatite (Cl^- substitution): a = 9.515 Å, c = 6.858 Å

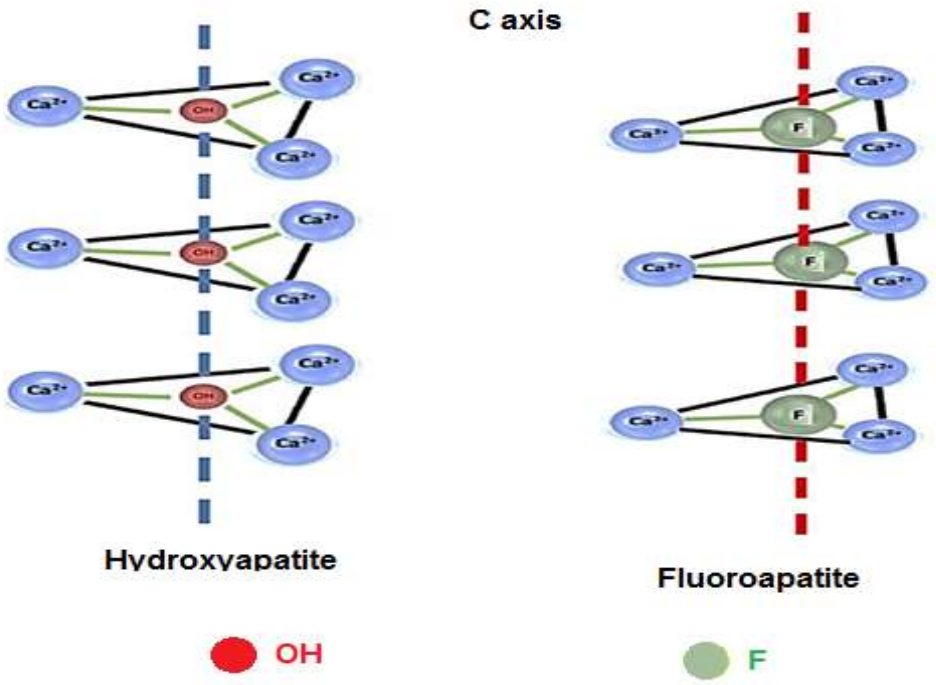

Figure I-9:Position of OH- and F- in Ca2 triangles - hydroxyapatite and fluoroapatite structures according to Ramadoss and Al *(Ramadoss et al., 2022)*

The following ions are generally known to be suitable for insertion into the apatite structure:

- For Ca^{2+} substitution: Mg^{2+}, Ba^{2+}, Pb^{2+} (among others) (Bystrov et al., 2023; Vasant, 2024; J. Wang, 2015)
- For $(PO_4)^{3-}$ substitution: $(BO_3)^{3-}$, vanadate, manganate, $(CO_3)^{2-}$, $(SiO_4)^{4-}$ (Deymier et al., 2017; H. Li et al., 2014; Suetsugu et al., 1998a)
- For (OH^-) substitution: F^-, Cl^-, $(CO_3)^{2-}$.(Madupalli et al., 2017; Piccoli & Candela, 2002; Suetsugu et al., 1998b)

The ion substitution in hydroxyapatite primarily influences the morphology of the crystals and the different properties of the various types of apatite (LeGeros, 1998).

5.3 Effect of Ca/P Ratio and Secondary Phases :

Calcium to Phosphorus (Ca/P) Ratio in Hydroxyapatite can also influences the apatite structure pyrophosphate ($Ca_2P_2O_7$). The molar ratio of Ca/P in synthetic hydroxyapatite is 1.667 (or Ca/P weight ratio = 2.151), whereas commercial Hap products typically exhibit ratios between 1.57 and 1.70. (Wolfram Holand, 2012)

Commonly observed secondary crystalline phases in non-stoichiometric Hap include:

- β-tricalcium phosphate ($Ca_3(PO_4)_2$)
- Tetra-calcium phosphate ($Ca_4P_2O_9$)
- Anhydrous dicalcium phosphate ($CaHPO_4$)
- Calcium pyrophosphate ($Ca_2P_2O_7$)

6. Synthetic Methods of Hydroxyapatite (Hap):

Numerous synthesis methods for hydroxyapatite (Hap) have been developed, each influencing the material's physical and chemical properties. These approaches are typically grouped into two main categories: the solid-state (dry) route and the wet-chemical (aqueous) route.

6.1 Solid-State Synthesis (dry method):

The solid-state synthesis of hydroxyapatite (Hap) involves the high-temperature calcination of stoichiometric mixtures of solid precursors, such as calcium carbonate, calcium hydroxide, and phosphate salts. Typically conducted at 900–1100 °C, this method yields highly crystalline and near-stoichiometric Hap powders. However, its major drawbacks include high energy consumption and the frequent formation of secondary phases (e.g., Hap/TCP or Hap/CaO), especially when the initial Ca/P ratio deviates from the ideal value of 1.67 (Rao et al., 1997).

6.2 Wet Chemical Methods:

6.2.1 Hydrothermal Method (Figure I-6) :

The hydrothermal method synthesizes hydroxyapatite by reacting calcium and phosphate precursors under high pressure and temperature in an autoclave (typically 200 °C for 45 hours) (Earl et al., 2006). It produces well-crystallized, single-phase HAP with controlled morphology, although residual counter-ions (e.g., Na^+) from precursors may alter surface properties and ionic substitution behaviour .

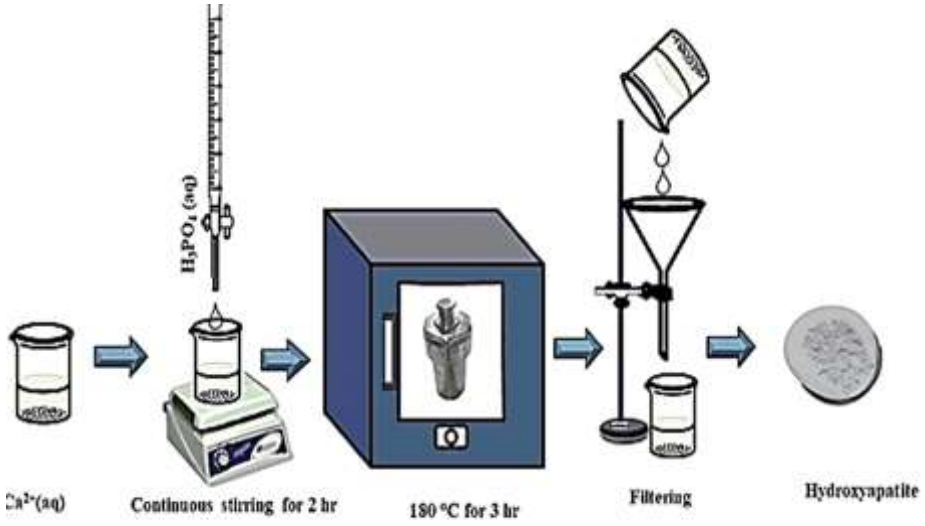

Figure I-10 :Synthesis of Hydroxyapatite by the Hydrothermal Method *(Kawsar et al., 2025)*

6.2.2 Sol-Gel Method (Figure I-7) :

The sol-gel method is a wet-chemical synthesis technique offering precise control over the composition and nanoscale morphology of hydroxyapatite. It involves the hydrolysis and polycondensation of metal alkoxides or salts to form a sol, which transitions into a gel. After drying and calcination, high-purity HAP with a large surface area is obtained. However, issues such as phosphate hydrolysis and the high cost of certain precursors may limit its applicability (Peng et al., 2012).

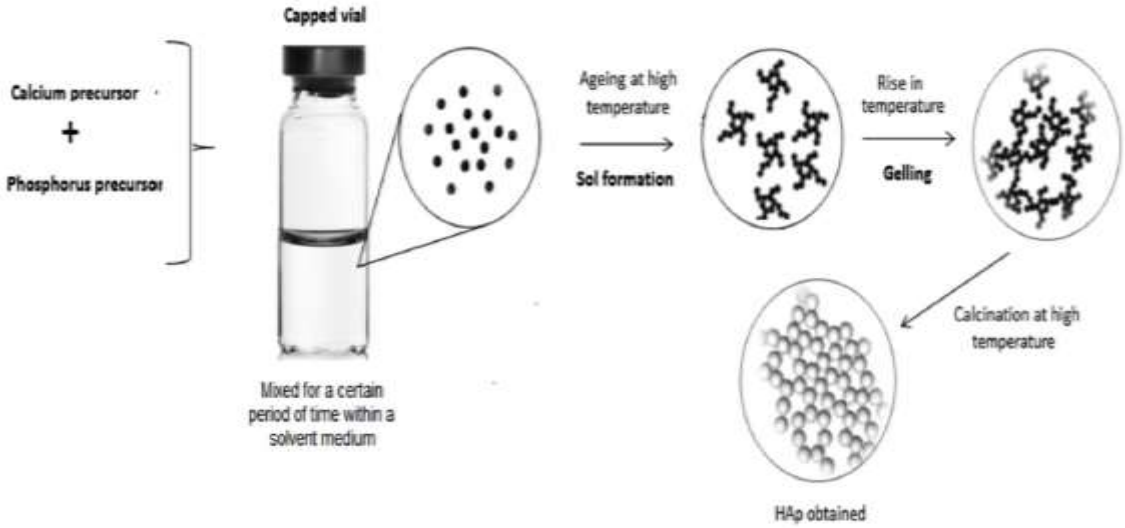

Figure I-11: Synthesis of Hydroxyapatite by Sol-Gel Method *(Gomes et al., 2019)*

6.2.3 Precipitation Method (figure I-8):

This is the most commonly used wet-chemical technique. It involves reacting calcium and phosphate ions in aqueous solution under controlled pH (typically between 9–11), temperature (25–100°C), and stirring conditions. The most frequently used precursors are $Ca(OH)_2$ and H_3PO_4 for direct neutralization, or $Ca(NO_3)_2$ and $(NH_4)_2HPO_4$ for double decomposition. Despite its versatility and scalability, reproducibility issues can arise due to its sensitivity to experimental parameters (Garcia, 2012).

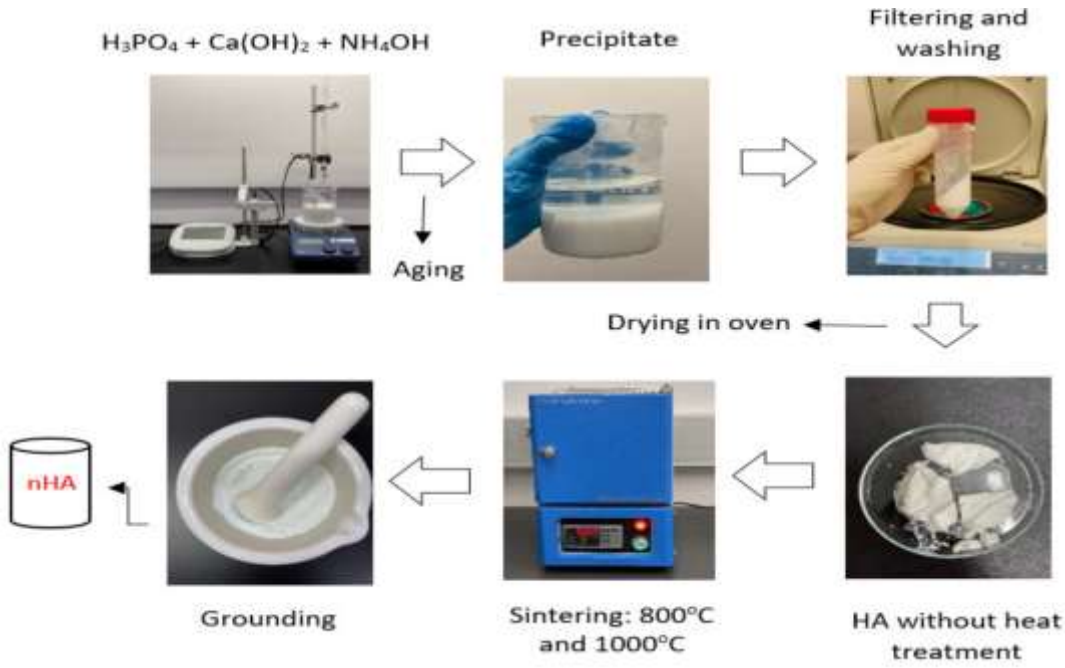

Figure I-8: Synthesis of Hydroxyapatite by precipitation Method *(Nguyen et al., 2023)*

7. Raw Material Alternatives for Hydroxyapatite Synthesis :

The Table 2 summarizes various waste materials utilized as alternative raw sources for the synthesis of hydroxyapatite. It outlines their origin, processing methods, resulting material characteristics, and potential applications.

Table I-2 : Overview of Waste-Derived Raw Materials for Hydroxyapatite Synthesis

Source Type	Raw Material	Processing Method(s)	HAp Characteristics	Applications / Notes	References
Mammalian Bone Waste	Bovine bone	Cleaning, defatting, calcination (750–1000 °C)	High purity, crystalline, Ca/P ≈ 1.67	Biomedical applications	(Jaber & Kovács, 2019; Odusote et al., 2019)
	Porcine bone	Calcination + ionic liquid	Ca/P: 1.49–1.54; rod-like particles (0.2–0.6 µm)	Nano-HAp potential	(Okpe et al., 2024)
	Caprine & ovine bones	Calcination	Nanostructured HAp	Bone tissue engineering	(Okpe et al., 2024)
Marine-Derived Waste	Fish bones and scales	Calcination (600–900 °C), alkaline hydrolysis	Ca/P: 1.47–2.63; rod/grain-shaped; trace elements (Mg, Na, K)	Enhanced biocompatibility	(Balabadra et al., 2024; Dermawan et al., 2022; Granito et al., 2018; Mustafa et al., 2015)
	Chicken eggshells	Precipitation, sol-gel, hydrothermal, microwave	High purity, Ca/P ≈ 1.67	Low-cost calcium source	(HamidiVadigh & Javadpour, 2024; Kareem & Eyiler, 2024; Muñoz-Sanchez et al., 2023; Peungsamran et al., n.d.)
	Oyster shells	Calcination (900–1200 °C) + reaction with phosphate	Mg, Sr trace elements; pure HAp	Biomedical-grade HAp	(Bhavan Ram et al., 2023; Rujitanapanich et al., 2014; Z. Wang et al., 2019)
	Mussel shells	Sol-gel, precipitation	Close to commercial Hap	Biomedical potential	(El-Bassyouni et al., 2020; Liandi et al., 2024; Muntean et al., 2024; Saragih et al., 2020)
	Cockle / scallop shells	Wet slurry precipitation	Morphology tunable via reaction time	Controlled synthesis	(Muntean et al., 2024)
	Snail shells	Calcination + acid treatment + hydrothermal	Bioactive, high-purity	Eco-friendly alternative	(Muntean et al., 2024)

	Crab & shrimp shells	Chitin + $CaCO_3$; precipitation, calcination	Hap–chitosan composites with superior structure	Bone regeneration	("Characterization of Hydroxyapatite Extracted from Crab Shell Using the Hydrothermal Method with Varying Holding Times," 2024;
Agricultural / Plant Waste	Rice husk	Partial hydrolysis + HAp coating	Silica-coated biomass composite	Wastewater treatment	(Aprillia et al., 2021; Zou et al., 2022)
	Coconut shell	Thermal / chemical (ongoing research)	–	Potential source	(Oladele et al., 2023)
	Eggshell + neem extract	Green synthesis	Size and morphology affected by plant template	Sustainable route	(HamidiVadigh & Javadpour, 2024; Kareem & Eyiler, 2024; Muñoz-Sanchez et al., 2023)

8. Hydroxyapatite Doping in Dental Implants and Coatings :

The crystalline structure and composition of Hap provide an excellent foundation for ionic doping, allowing for the incorporation of various dopant ions that can enhance specific biological and mechanical properties (Tosan et al., 2021). Pure Hap coatings have been extensively used to improve the osseointegration of metallic implants with surrounding bone tissue, but they often lack certain functional properties such as antimicrobial activity and enhanced osteoinductivity (Islam et al., 2025).

The doping process involves introducing foreign ions into the Hap crystal lattice, fundamentally altering the material's physicochemical and biological characteristics (Kubiak-Mihkelsoo et al., 2025a). This ionic doping strategy has emerged as a promising approach to bridge the gap between synthetic biomaterials and native bone tissue, providing customized solutions for clinical applications (J. Li et al., 2023). The most common dopants include cationic ions such as zinc (Zn^{2+}), magnesium (Mg^{2+}), strontium (Sr^{2+}), and silver (Ag^{+}), as well as anionic dopants like fluoride (F^{-}) (Tosan et al., 2021) (Kubiak-Mihkelsoo et al., 2025b)

The table 3 shows the commonly used dopant ions in hydroxyapatite-based dental coatings. It highlights their methods of incorporation, resulting physicochemical and biological modifications.

Table I-3: Summary of Ionic Doping in Hydroxyapatite for Dental Applications

Dopant Ion	Incorporation Method	Structural Effects	Biological Effects	Applications	References
Zinc (Zn^{2+})	Substitution in Hap lattice via sol-gel or precipitation	Alters crystallinity, lattice, solubility, and surface morphology	Enhances osteoblast proliferation & antimicrobial properties	Bone regeneration, antibacterial dental coatings	(Dornelas et al., 2024; Islam et al., 2025)
Silver (Ag^{+})	Wet precipitation or ion exchange	Replaces Ca^{2+}, sustained Ag^{+} release	Broad-spectrum antimicrobial without cytotoxicity (at low dose)	Antibacterial coatings for dental implants	(Iconaru et al., 2014)
Strontium (Sr^{2+})	Substitution into Hap lattice	Causes anisotropic lattice expansion along c-axis	Promotes odontogenic differentiation; non-cytotoxic	Remineralization, enamel repair, stem cell compatibility	(Rajendran & Antony, 2023)

Magnesium (Mg^{2+})	Doping at 5–7 mol% via precipitation or thermal treatment	Reduces crystallinity, modifies a and c lattice parameters	Improves strength; supports cell adhesion; antibacterial	Tougher dental coatings with bioactivity	(Mansour et al., 2017)
Fluoride (F^-)	Replaces OH^- groups in HA to form FHA	Improves chemical and acid resistance	Enhances stem cell attachment; dual-doping with Zn^{2+} boosts antibacterial effect	Caries prevention, implant coatings	(*Application of Fluoridated Hydroxyapatite Thin Film Coatings Using KrF Pulsed Laser Deposition*, n.d.)

9. Antibacterial Activity in Dental Ceramic Coatings:

The incorporation of antibacterial properties into dental materials is critical for preventing microbial colonization and consequent infection in the oral cavity. Dental restorations and implant surfaces are continuously exposed to a diverse microbiota, including *Streptococcus mutans* and *Staphylococcus aureus*, which can adhere, proliferate, and ultimately compromise the longevity of the restoration or implant (Gubatan et al. 2020). The acidic metabolic by-products of these bacteria can lead to secondary caries, mucositis, and peri-implantitis, necessitating revisions or replacements that burden both patients and healthcare systems (Morales Espino et al. 2024).

9.1 Bacterial Interaction and Biofilm Formation :

Upon exposure to an implant surface, planktonic bacteria initially adhere through reversible physicochemical interactions, influenced by surface roughness, wettability, and free energy(Damm et al. 2017). Rough or hydrophobic surfaces afford protective niches that facilitate irreversible attachment and extracellular polymeric substance (EPS) production, culminating in a mature biofilm structure (Tsuneda et al. 2003). This biofilm matrix impedes host immune responses and acts as a diffusion barrier against therapeutic agents, rendering infections recalcitrant to treatment (Shi et al. 2020).

9.2 Antibacterial Coatings :

To mitigate biofilm-associated complications, the development of antibacterial coatings has become paramount. Such coatings aim to inhibit initial adhesion, disrupt EPS synthesis, or kill bacteria upon contact, thereby reducing infection risk and extending the functional lifespan of dental devices (Zhai et al. 2023). Antibacterial strategies include incorporation of metal ions, organic biocides, or immobilized antimicrobial polymers. Among these, ceramic coatings offer favorable mechanical properties and chemical stability essential for load-bearing applications (Wang et al. 2014).

9.3 Evaluation: Zone of Inhibition Test :

Antibacterial efficacy of coatings is commonly assessed via the zone of inhibition assay (Zone of Inhibition n.d.). In this method, coated substrates are placed on agar plates inoculated with target bacteria; diffusion of antimicrobial species from the coating creates a clear halo where bacterial growth is inhibited (Tchaou et al. 1996). Measurement of the halo diameter provides a quantitative metric for comparative evaluation of antibacterial activity across different material formulations(Zhang et al. 2020)

References :

Abraham, A., & Venkatesan, S. (2022). A review on application of biomaterials for medical and dental implants. *Proceedings of the Institution of Mechanical Engineers, Part L: Journal of Materials: Design and Applications, 237*(2), 249–273.

Agustín-Panadero, R., Román-Rodríguez, J. L., Ferreiroa, A., Solá-Ruíz, M. F., & Fons-Font, A. (2014). Zirconia in fixed prosthesis: A literature review. *Journal of Clinical and Experimental Dentistry, 6*(1), e66–e73. https://doi.org/10.4317/jced.51304

Alsahafi, R. A., Mitwalli, H. A., Balhaddad, A. A., Weir, M. D., Xu, H. H., & Melo, M. A. (2021). Regenerating craniofacial dental defects with calcium phosphate cement scaffolds: Current status and innovative scope review.

Anusavice, K. J. (2012). *Phillips' science of dental materials*. Elsevier.

Application of fluoridated hydroxyapatite thin film coatings using KrF pulsed laser deposition. (n.d.). Retrieved June 18, 2025, from https://www.jstage.jst.go.jp/article/dmj/37/3/37_2017-122/_article/-char/en

Aprillia, I., Suprastiwi, E., Megantoro, A., Trisna, L. P., Utami, B., & Yana, S. (2021). The effect of rice husk nanosilica hydroxyl compound on dentin biomineralization. *Journal of Advanced Pharmaceutical Technology & Research, 12*(3), 227–231. https://doi.org/10.4103/japtr.JAPTR_227_21

Balabadra, K. M., Panneer Selvam, S., Ramadoss, R., & Sundar, S. (2024). Hydroxyapatite synthesis and characterization from marine sources: A comparative study. *Journal of Oral Biology and Craniofacial Research, 14*(6), 706–711. https://doi.org/10.1016/j.jobcr.2024.09.009

Bhavan Ram, U., Sujatha, V., Vidhya, S., Jayasree, R., & Mahalaxmi, S. (2023). Oyster shell-derived nano-hydroxyapatite and proanthocyanidin pretreatment on dentinal tubule occlusion and permeability before and after acid challenge—An in vitro study. *Journal of Materials Science: Materials in Medicine, 34*(4), 17. https://doi.org/10.1007/s10856-023-06724-4

Bystrov, V. S., Paramonova, E. V., Avakyan, L. A., Eremina, N. V., Makarova, S. V., & Bulina, N. V. (2023). Effect of magnesium substitution on structural features and properties of hydroxyapatite. *Materials, 16*(17), 5945. https://doi.org/10.3390/ma16175945

Characterization of hydroxyapatite extracted from crab shell using the hydrothermal method with varying holding times. (2024). *Journal of Renewable Materials, 12*(6), 1145–1163. https://doi.org/10.32604/jrm.2024.052165

Della Bona, A., Pecho, O. E., & Alessandretti, R. (2015). Zirconia as a dental biomaterial. *Materials, 8*(8), 4978–4991.

Dermawan, S. K., Ismail, Z. M. M., Jaffri, M. Z., & Abdullah, H. Z. (2022). Extraction and characterization of natural hydroxyapatite from black tilapia fish bone for biomedical applications. *Key Engineering Materials, 908*, 159–164. https://doi.org/10.4028/p-3j8b8t

Deymier, A. C., Nair, A. K., Depalle, B., Qin, Z., Arcot, K., Drouet, C., Yoder, C. H., Buehler, M. J., Thomopoulos, S., Genin, G. M., & Pasteris, J. D. (2017). Protein-free formation of bone-like apatite: New insights into the key role of carbonation. *Biomaterials, 127*, 75–88. https://doi.org/10.1016/j.biomaterials.2017.02.029

Dornelas, J., Dornelas, G., Rossi, A., Piattelli, A., Di Pietro, N., Romasco, T., Mourão, C. F., & Alves, G. G. (2024). The incorporation of zinc into hydroxyapatite and its influence on the cellular response to biomaterials: A systematic review. *Journal of Functional Biomaterials, 15*(7), 178. https://doi.org/10.3390/jfb15070178

dos Santos, V. I., Chevalier, J., Fredel, M. C., Henriques, B., & Gremillard, L. (2024). Ceramics and ceramic composites for biomedical engineering applications via direct ink writing: Overall scenario, advances in the improvement of mechanical and biological properties and innovations. *Materials Science and Engineering: R: Reports, 161*, 100841. https://doi.org/10.1016/j.mser.2024.100841

Earl, J. S., Wood, D. J., & Milne, S. J. (2006). Hydrothermal synthesis of hydroxyapatite.

El-Bassyouni, G. T., Eldera, S. S., Kenawy, S. H., & Hamzawy, E. M. A. (2020). Hydroxyapatite nanoparticles derived from mussel shells for in vitro cytotoxicity test and cell viability. *Heliyon, 6*(6), e04085. https://doi.org/10.1016/j.heliyon.2020.e04085

Elliott, J. C. (1994). *Structure and chemistry of the apatites and other calcium orthophosphates*. Elsevier.

Franzén, A., Hultenby, K., Reinholt, F. P., Önnerfjord, P., & Heinegård, D. (2008). Altered osteoclast development and function in osteopontin deficient mice. *Journal of Orthopaedic Research, 26*(5), 721–728.

Garcia, S. D. (2012). *Les hydroxyapatites, un système basique atypique modulable par la synthèse: Vers l'identification des sites actifs* (Doctoral dissertation, Université Pierre et Marie Curie – Paris VI).

Gomes, D. S., Santos, A. M., Neves, G. A., & Menezes, R. R. (2019). A brief review on hydroxyapatite production and use in biomedicine. *Cerâmica, 65*(374), 282–302.

Gopi, D., Bhalaji, P. R., Prakash, V. C., Ramasamy, A. K., Kavitha, L., & Ferreira, J. M. (2011). An effective and facile synthesis of hydroxyapatite powders using oxalic acid–ethylene glycol mixture. *Current Applied Physics, 11*(3), 590–593.

Gopi, D., Indira, J., Kavitha, L., Sekar, M., & Mudali, U. K. (2012). Synthesis of hydroxyapatite nanoparticles by a novel ultrasonic-assisted mixed hollow sphere template method. *Spectrochimica Acta Part A: Molecular and Biomolecular Spectroscopy, 93*, 131–134.

Granito, R. N., Muniz Renno, A. C., Yamamura, H., de Almeida, M. C., Menin Ruiz, P. L., & Ribeiro, D. A. (2018). Hydroxyapatite from fish for bone tissue engineering: A promising approach. *International Journal of Molecular and Cellular Medicine, 7*(2), 80–90. https://doi.org/10.22088/IJMCM.BUMS.7.2.80

Gupta, K., Kaushi, N., Sharma, V., & Singh, A. (2025). A review on innovations in hydroxyapatite: Advancing sustainable and multifunctional dental implants. *Odontology*, 1–13.

HamidiVadigh, F., & Javadpour, J. (2024). The synthesis of hydroxyapatite nanoparticles using eggshells and two different phosphate sources. *European Journal of Engineering and Technology Research, 9*(2). https://doi.org/10.24018/ejeng.2024.9.2.3151

Iconaru, S. L., Chapon, P., Le Coustumer, P., & Predoi, D. (2014). Antimicrobial activity of thin solid films of silver-doped hydroxyapatite prepared by sol–gel method. *The Scientific World Journal, 2014*, 165351. https://doi.org/10.1155/2014/165351

Islam, M. A., Hossain, N., Hossain, S., Khan, F., Hossain, S., Arup, M. M. R., Chowdhury, M. A., & Rahman, M. M. (2025). Advances of hydroxyapatite nanoparticles in dental implant applications. *International Dental Journal, 75*(3), 2272–2313. https://doi.org/10.1016/j.identj.2024.11.020

Jaber, H. L., & Kovács, T. A. (2019). Preparation and synthesis of hydroxyapatite bioceramic from bovine bone by thermal heat treatment. *Építőanyag – Journal of Silicate Based and Composite Materials, 71*(3), 98–101. https://doi.org/10.14382/epitoanyag-jsbcm.2019.18

Kandori, K., Hamazaki, H., Matsuzawa, M., & Togashi, S. (2014). Selective adsorption of acidic protein of bovine serum albumin onto sheet-like calcium hydroxyapatite particles produced by microreactor. *Advanced Powder Technology, 25*(1), 354–359.

Kandori, K., Toshima, S., Wakamura, M., Fukusumi, M., & Morisada, Y. (2010). Effects of modification of calcium hydroxyapatites by trivalent metal ions on the protein adsorption behavior. *The Journal of Physical Chemistry B, 114*(7), 2399–2404.

Kareem, Z., & Eyiler, E. (2024). Synthesis of hydroxyapatite from eggshells via wet chemical precipitation: A review. *RSC Advances, 14*(30), 21439–21452. https://doi.org/10.1039/D4RA02198C

Kawsar, M., Hossain, M. S., Bahadur, N. M., Islam, D., & Ahmed, S. (2025). Crystalline structure modification of hydroxyapatite via a hydrothermal method using different modifiers. *Materials Advances*.

Kubiak-Mihkelsoo, Z., Kostrzębska, A., Błaszczyszyn, A., Pitułaj, A., Dominiak, M., Gedrange, T., Nawrot-Hadzik, I., Matys, J., & Hadzik, J. (2025a). Ionic doping of hydroxyapatite for bone regeneration: Advances in structure and properties over two decades—A narrative review. *Applied Sciences, 15*(3), 1108. https://doi.org/10.3390/app15031108

Kubiak-Mihkelsoo, Z., Kostrzębska, A., Błaszczyszyn, A., Pitułaj, A., Dominiak, M., Gedrange, T., Nawrot-Hadzik, I., Matys, J., & Hadzik, J. (2025b). Ionic doping of hydroxyapatite for bone regeneration: Advances in structure and properties over two decades—A narrative review. *Applied Sciences, 15*(3), 1108. https://doi.org/10.3390/app15031108

LeGeros, R. A. (1998). [Incomplete reference – add title and publisher].

Li, H., Baikie, T., Pramana, S. S., Shin, J. F., Keenan, P. J., Slater, P. R., Brink, F., Hester, J., An, T., & White, T. J. (2014). Hydrothermal synthesis, structure investigation, and oxide ion

conductivity of mixed Si/Ge-based apatite-type phases. *Inorganic Chemistry, 53*(10), 4803–4812. https://doi.org/10.1021/ic402370e

Li, J., Zhang, T., Liao, Z., Wei, Y., Hang, R., & Huang, D. (2023). Engineered functional doped hydroxyapatite coating on titanium implants for osseointegration. *Journal of Materials Research and Technology, 27*, 122–152. https://doi.org/10.1016/j.jmrt.2023.09.239

Liandi, A. R., Rianom, W. H., Cahyana, A. H., Fathoni, A., & Wendari, T. P. (2024). Transforming seafood waste: Green mussel shell-derived hydroxyapatite as a catalyst for spirooxindole synthesis. *Bioresource Technology Reports, 25*, 101796. https://doi.org/10.1016/j.biteb.2024.101796

Madupalli, H., Pavan, B., & Tecklenburg, M. M. J. (2017). Carbonate substitution in the mineral component of bone: Discriminating the structural changes simultaneously imposed by carbonate in A and B sites of apatite. *Journal of Solid State Chemistry, 255*, 27–35. https://doi.org/10.1016/j.jssc.2017.07.025

Mansour, S. F., El-Dek, S. I., Dorozhkin, S. V., & Ahmed, M. K. (2017). Physico-mechanical properties of Mg- and Ag-doped hydroxyapatite/chitosan biocomposites. *New Journal of Chemistry, 41*(22), 13773–13783. https://doi.org/10.1039/C7NJ01777D

Misch, C. E. (2007). *Contemporary implant dentistry*. Mosby.

Muñoz-Sanchez, E. R., Arrieta-Gonzalez, C. D., Quinto-Hernandez, A., Garcia-Hernandez, E., & Porcayo-Calderon, J. (2023). Synthesis of hydroxyapatite from eggshell and its electrochemical characterization as a coating on titanium. *International Journal of Electrochemical Science, 18*(9), 100204. https://doi.org/10.1016/j.ijoes.2023.100204

Muntean, F. L., Olariu, I., Marian, D., Olariu, T., Petrescu, E. L., Olariu, T., & Drăghici, G. A. (2024). Hydroxyapatite from mollusk shells: Characteristics, production, and potential applications in dentistry. *Dentistry Journal*, *12*(12), 409. https://doi.org/10.3390/dj12120409

Mustafa, N., Ibrahim, M. H. I., Asmawi, R., & Amin, A. M. (2015). Hydroxyapatite extracted from waste fish bones and scales via calcination method. *Applied Mechanics and Materials, 773–774*, 287–290. https://doi.org/10.4028/www.scientific.net/AMM.773-774.287

Nguyen, N. M., Kakarla, A. B., Nukala, S. G., Kong, C., Baji, A., & Kong, I. (2023). Evaluation of physicochemical properties of a hydroxyapatite–polymer nanocomposite for use in fused filament fabrication. *Polymers, 15*(19), 3980.

Odusote, J. K., Danyuo, Y., Baruwa, A. D., & Azeez, A. A. (2019). Synthesis and characterization of hydroxyapatite from bovine bone for production of dental implants. *Journal of Applied Biomaterials & Functional Materials, 17*(2), 2280800019836829. https://doi.org/10.1177/2280800019836829

Okpe, P. C., Folorunso, O., Aigbodion, V. S., & Obayi, C. (2024). Hydroxyapatite synthesis and characterization from waste animal bones and natural sources for biomedical applications. *Journal of Biomedical Materials Research Part B: Applied Biomaterials, 112*(7), e35440. https://doi.org/10.1002/jbm.b.35440

Oladele, I. O., Taiwo, A. S., Onuh, L. N., Adelani, S. O., Balogun, S. O., Lephuthing, S. S., & Olubambi, P. A. (2023). Characterization of animal shells-derived hydroxyapatite reinforced epoxy bio-composites. *Composites and Advanced Materials, 32*, 26349833231223984. https://doi.org/10.1177/26349833231223984

Peng, F., Veilleux, E., Schmidt, M., & Wei, M. (2012). Synthesis of hydroxyapatite nanoparticles with tailorable morphologies and carbonate substitutions using a wet precipitation method. *Journal of Nanoscience and Nanotechnology, 12*(3), 2774–2782.

Peungsamran, N., Chumee, J., & Poomipeng, A. (n.d.). Synthesis and characterization of hydroxyapatite from biowaste eggshells for medical application.

Piccoli, P. M., & Candela, P. A. (2002). Apatite in igneous systems. *Reviews in Mineralogy and Geochemistry, 48*(1), 255–292. https://doi.org/10.2138/rmg.2002.48.6

Prasad Kumara, P., Cooper, P., Cathro, P., Gould, M., Dias, G., & Ratnayake, J. (2025). Bioceramics in endodontics: Limitations and future innovations—A review. *Dentistry Journal, 13*(4), 157.

Quillard, S., Paris, M., Deniard, P., Gildenhaar, R., Berger, G., Obadia, L., & Bouler, J. M. (2011). Structural and spectroscopic characterization of a series of potassium- and/or sodium-substituted β-tricalcium phosphate. *Acta Biomaterialia, 7*(4), 1844–1854.

Rajendran, R., & Antony, D. P. (2023). Development and elemental analysis of a novel strontium-doped nano-hydroxyapatite paste and evaluation of its remineralization potential: An in vitro study. *Cureus*. https://doi.org/10.7759/cureus.48650

Ramadoss, R., Padmanaban, R., & Subramanian, B. (2022). Role of bioglass in enamel remineralization: Existing strategies and future prospects—A narrative review. *Journal of Biomedical Materials Research Part B: Applied Biomaterials, 110*(1), 45–66.

Rao, R., Roopa, H., & Kannan, T. (1997). Solid state synthesis and thermal stability of HAP and HAP–β-TCP composite ceramic powders. *Journal of Materials Science: Materials in Medicine, 8*(8), 511–518.

Rivera-Muñoz, E. M. (2011). Hydroxyapatite-based materials: Synthesis and characterization.

Rujitanapanich, S., Kumpapan, P., & Wanjanoi, P. (2014). Synthesis of hydroxyapatite from oyster shell via precipitation. *Energy Procedia, 56*, 112–117. https://doi.org/10.1016/j.egypro.2014.07.138

Sáenz, A., Rivera-Muñoz, E.M., Brostow, W., & Castaño, V.M. (1999). CERAMIC BIOMATERIALS: AN INTRODUCTORY OVERVIEW.

Sakaguchi, R. L. (2012). *Craig's restorative dental materials*. Elsevier.

Saragih, A. S., Pamungkas, A., & Noviyanto, A. (2020). Synthesis of hydroxyapatite from Indonesian green mussels (*Perna viridis*) via precipitation methods. *Key Engineering Materials, 833*, 199–203. https://doi.org/10.4028/www.scientific.net/KEM.833.199

Schmalz, G., & Arenholt-Bindslev, D. (2009). *Biocompatibility of dental materials* (Vol. 1). Springer.

Suetsugu, Y., Shimoya, I., & Tanaka, J. (1998a). Configuration of carbonate ions in apatite structure determined by polarized infrared spectroscopy. *Journal of the American Ceramic Society, 81*(3), 746–748. https://doi.org/10.1111/j.1151-2916.1998.tb02403.x

Suetsugu, Y., Shimoya, I., & Tanaka, J. (1998b). Configuration of carbonate ions in apatite structure determined by polarized infrared spectroscopy. *Journal of the American Ceramic Society, 81*(3), 746–748. https://doi.org/10.1111/j.1151-2916.1998.tb02403.x

Szcześ, A., Hołysz, L., & Chibowski, E. (2017). Synthesis of hydroxyapatite for biomedical applications. *Advances in Colloid and Interface Science, 249*, 321–330.

Tosan, F., Rahnama, N., Sakhaei, D., Fathi, A. H., & Yari, A. (2021). Effects of doping metal nanoparticles in hydroxyapatite in improving the physical and chemical properties of dental implants. *Nanomedicine Research Journal, 6*(4), 327–336. https://doi.org/10.22034/nmrj.2021.04.002

Tsetsekou, A., Brasinika, D., Vaou, V., & Chatzitheodoridis, E. (2014). On the synthesis of tailored biomimetic hydroxyapatite nanoplates through a bioinspired approach in the presence of collagen or chitosan and L-arginine. *Materials Science and Engineering: C, 43*, 555–565.

Vasant, S. R. (2024). Synthesis and characterization of pure and magnesium-ion-doped CPPD nanoparticles. *The Scientific Temper, 15*(2). https://doi.org/10.58414/SCIENTIFICTEMPER.2024.15.2.56

Wang, J. (2015). Incorporation of iodine into apatite structure: A crystal chemistry approach using artificial neural network. *Frontiers in Earth Science, 3*. https://doi.org/10.3389/feart.2015.00020

Wang, Z., Jiang, S., Zhao, Y., & Zeng, M. (2019). Synthesis and characterization of hydroxyapatite nanorods from oyster shell with exogenous surfactants. *Materials Science and Engineering: C, 105*, 110102. https://doi.org/10.1016/j.msec.2019.110102

Williams, D. F. (2008). On the mechanisms of biocompatibility. *Biomaterials, 29*(20), 2941–2953. https://doi.org/10.1016/j.biomaterials.2008.04.023

Wolfram Holand, G. H. (2012). *Glass ceramic technology*. Wiley.

Yelten-Yilmaz, A., & Yilmaz, S. (2018). Wet chemical precipitation synthesis of hydroxyapatite (HA) powders. *Ceramics International, 44*(8), 9703–9710.

Zou, C., Guan, K., Nie, F., Sun, X., & Liu, W. (2022). Optimized preparation of hydroxyapatite-modified carbonized rice husk and its adsorption property for Cr(VI) ions. *Desalination and Water Treatment, 271*, 192–205. https://doi.org/10.5004/dwt.2022.28808

Damm, M., Holm, C., Blaabjerg, M., Bro, M. N., & Schwarz, D. (2017). Differential somatic cell count—a novel method for routine mastitis screening in the frame of dairy herd improvement testing programs. *Journal of Dairy Science, 100*(6), 4926–4940. https://doi.org/10.3168/jds.2016-12409

Gubatan, J., Mehigan, G. A., Villegas, F., Mitsuhashi, S., Longhi, M. S., Malvar, G., Csizmadia, E., Robson, S., & Moss, A. C. (2020). Cathelicidin mediates a protective role of vitamin D in ulcerative colitis and human colonic epithelial cells. *Inflammatory Bowel Diseases, 26*(6), 885–897. https://doi.org/10.1093/ibd/izz330

Morales Espino, A., Déniz, S., Fumero-Hernández, M., Encinoso, M., Calabuig, P., Conde-Felipe, M., & Jaber, J. R. (2024). A cadaveric study using anatomical cross-section and computed tomography for the coelomic cavity in juvenile Cory's shearwater (Aves, Procellariidae, *Calonectris borealis*). *Animals, 14*(6), 858. https://doi.org/10.3390/ani14060858

Shi, C., Miller, B. R., Alexander, E. M., Gulick, A. M., & Aldrich, C. C. (2020). Design, synthesis, and biophysical evaluation of mechanism-based probes for condensation domains of nonribosomal peptide synthetases. *ACS Chemical Biology, 15*(7), 1813–1819. https://doi.org/10.1021/acschembio.0c00411

Tchaou, W. S., Turng, B. F., Minah, G. E., & Coll, J. A. (1996). Inhibition of pure cultures of oral bacteria by root canal filling materials. *Pediatric Dentistry, 18*(7), 444–449.

Tsuneda, S., Aikawa, H., Hayashi, H., Yuasa, A., & Hirata, A. (2003). Extracellular polymeric substances responsible for bacterial adhesion onto solid surface. *FEMS Microbiology Letters, 223*(2), 287–292. https://doi.org/10.1016/S0378-1097(03)00399-9

Wang, R.-R., Lu, C.-L., Wang, G., & Zhang, D.-S. (2014). Influence of cyclic loading on the fracture toughness and load bearing capacities of all-ceramic crowns. *International Journal of Oral Science, 6*(2), 99–104. https://doi.org/10.1038/ijos.2013.94

Zhai, S., Tian, Y., Shi, X., Liu, Y., You, J., Yang, Z., Wu, Y., & Chu, S. (2023). Overview of strategies to improve the antibacterial property of dental implants. *Frontiers in Bioengineering and Biotechnology, 11*, 1267128. https://doi.org/10.3389/fbioe.2023.1267128

Zhang, J., Tang, Q., Chen, W., Sun, H., Ou, Q., & Wen, Y. (2020). An improved halo method for evaluating the antibacterial activity of leather. *Leather and Footwear Journal, 20*(3), 229–236. https://doi.org/10.24264/lfj.20.3.2

Zone of inhibition. (n.d.). Retrieved November 7, 2025, from https://www.nelsonlabs.com/testing/zone-of-inhibition/

Chapter II : Experimental protocols

Chapter II: Experimental protocols

1. Introduction:

The second chapter outlines the experimental methodologies employed for the synthesis and physicochemical characterization of the materials investigated in this study.

Structural analysis was performed using X-ray diffraction (XRD) to determine the crystalline phases present. Complementary techniques, including particle size distribution assessment, were conducted to evaluate key physical properties of the materials. Furthermore, Fourier-transform infrared spectroscopy (FTIR) was used to probe the functional groups and chemical structure of the developed hydroxyapatite formulations.

All characterization procedures were carried out within the facilities of the Process Engineering Department, the LTPO Laboratory, and the Quality Control Laboratory of the Hassasna Cement Plant.

2. Humidity (Latimer, et al., 2023):

The humidity (moisture content) of a material sample is determined by measuring the loss in weight after drying the sample at a controlled temperature. This method is based on the principle that water present in the sample will evaporate when heated, while the dry matter remains unchanged. The decrease in weight after drying corresponds to the amount of water originally present in the sample

- **Procedure :**

To determine humidity, place about 2 grams of the sample on a watch glass and record its initial weight (Wwet). Dry the sample in an oven (figure II-1) at 105°C for 24 hours, then cool and weigh it to obtain the dry weight (Wdry). Repeat drying and weighing every 30 minutes until the weight no longer changes. Calculate humidity as:

$$\text{Humidity (\%)} = W_{wet} - W_{dry} / W_{wet} * 100 \quad \text{(1)}$$

Figure II-1: Memmert Drying Oven used during Humidity Test

3. Loss on Ignition (LOI) :

The principle of the Loss on Ignition (LOI) method is to determine the amount of volatile substances (such as water, carbon dioxide, and organic matter) present in a sample by measuring the mass lost when the sample is heated to a high temperature. When heated in a crucible at 950°C, these volatile components are released and the decrease in mass reflects their total content. The difference in mass before and after heating, expressed as a percentage, represents the LOI.

- ***Procedure*** (NA235-2001, 2001) ***:***

A clean, dry crucible is weighted. Exactly 1 g of the sample is added to the crucible. W1 (in grams) the combined mass of the crucible and sample is recorded. The crucible with the sample is placed in a calciner (figure II-2) and heated at 950°C for 45 minutes. After heating, the crucible is removed and allowed to cool to room temperature in a desiccator to prevent moisture absorption.

Once cooled, the crucible is weighted again and the mass is recorded as W2 (in grams).

The Loss on Ignition (LOI) percentage is calculated using the following formula:

$$\text{LOI } (\%) = \frac{W1\text{-}W2}{W1} \times 100 \ldots\ldots\ldots\ldots\ldots \textbf{(2)}$$

Where:

W1: mass of crucible with 1 g of sample (g)

W2: mass of cooled crucible after ignition (g).

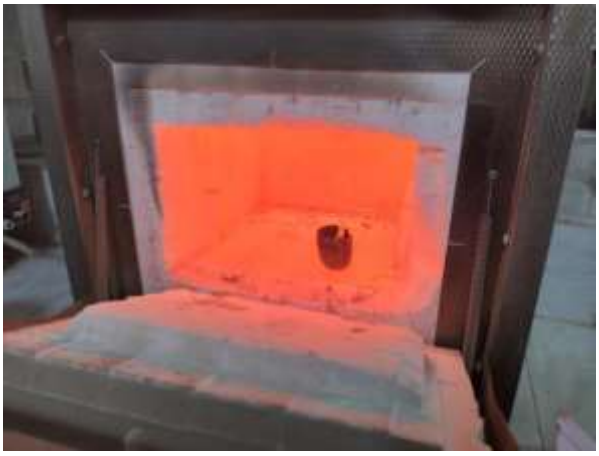

Figure II-2: Muffle Furnace (Calciner)

4. X-ray fluorescence spectrometry (NA5042., 2014.):

X-ray fluorescence (XRF) spectrometry is a highly effective analytical technique for determining the elemental composition of materials. In this method, samples typically prepared as compressed pellets are exposed to incident X-ray radiation. The interaction of the primary X-rays with the sample's atoms induces the emission of secondary, element-specific X-rays as a result of electronic excitation and subsequent relaxation processes. By detecting and quantifying these characteristic secondary emissions, the XRF spectrometer enables precise identification and quantification of the constituent elements within the sample

For our analyses, we employ the PANalytical ZETIUM X-ray fluorescence spectrometer (Figure II-3)

Figure II-3:X-ray fluorescence spectrometer PAN analytical ZETIUM

5. Energy Dispersive X-ray Spectroscopy :

Energy-Dispersive X-ray Spectroscopy (EDS) works by using a focused electron beam to remove inner-shell electrons from atoms in the sample. When outer-shell electrons fill these vacancies, they emit characteristic X-rays. These X-rays are detected by a silicon drift detector and converted into an energy spectrum. Each peak in the spectrum corresponds to an element, allowing simple elemental identification and semi-quantitative analysis. The sample is cleaned, dried, and mounted on a conductive stub, and non-conductive materials are coated to prevent charging before analysis.

6. X-ray diffraction :

X-Ray Diffraction (XRD) is a powerful analytical technique based on the constructive interference of monochromatic X-rays with crystalline samples, governed by Bragg's Law ($n\lambda = 2d \sin\theta$). When X-rays encounter regularly arranged atoms in a crystal lattice, they produce characteristic diffraction patterns that serve as unique fingerprints for phase identification and structural analysis. For analysis, samples are ground into fine powders (1-100 μm) and mounted in holders to ensure random crystallite orientation. Data collection employs a diffractometer with Cu Kα radiation ($\lambda = 1.5406$ Å), scanning across 2θ angles typically from 10° to 80° with 0.02° step increments.

7. Infrared Spectroscopy :

IR spectroscopy relies on the absorption of specific infrared frequencies by molecular bonds, corresponding to vibrational energy transitions. When IR radiation (wavenumber range: 4,000–400 cm^{-1}) interacts with a sample, bonds undergo stretching, bending, or twisting motions if the vibration alters the molecule's dipole moment, these absorbed frequencies produce a unique spectral "fingerprint," with two key regions: the functional group region and the fingerprint region. The functional group region provides information about the presence of specific functional groups, while the fingerprint region contains complex absorption patterns unique to individual compounds, enabling precise identification.

8. Granulometric Analysis by Sieve Shaking (ASTM International, 2018):

Granulometric analysis determines the particle size distribution of a material by mechanically separating particles through series of sieves with progressively smaller mesh openings. The method is based on the principle that particles larger than the sieve aperture are retained on the sieve, while smaller particles pass through. By weighing the material retained on each sieve,

the percentage distribution of different particle size fractions can be calculated, providing valuable information about the material's physical properties.

- ***Procedure***

First, weigh exactly 100 g of the dried sample using an analytical balance and record the initial sample weight. Next, clean all sieves and the collection pan thoroughly, then weigh each empty sieve individually and record their initial weights. After preparation, arrange the sieves in descending order of mesh size, placing the largest mesh sieve on top (figure II-4)

Figure II-4 : Sieve Stack Assembly

Pour the 100 g sample onto the top sieve (106 μm) and secure the entire sieve stack on the sieve shaker. Operate the shaker for 10–15 minutes at the appropriate amplitude and frequency, then stop the shaker and carefully disassemble the stack (figure II-5). Weigh each sieve with the retained material and record the final weights. The weight of material retained on each sieve is determined by subtracting the initial sieve weight from the final weight. Finally, weigh the material collected in the bottom pan.

The percentage retained in each sieve is calculated as followed:

Weight retained on each sieve = Final weight - Initial weight…….(3)

Percentage retained = (Weight retained / Total sample weight) × 100…….(4)

Figure II-5 : Ro-Tap Sieve Shaker

9. Hydrogen potential (pH) measurement and Conductivity measurement (Day, 1965):

This wet analysis method determines suspension stability by monitoring pH and conductivity changes during controlled agitation. The principle relies on observing electrochemical stabilization as particles interact with water, where consistent pH and conductivity readings indicate equilibrium between soluble components and suspended particles.

- ***Procedure***

Prepare a 20g sample in a 100ml beaker, add 50ml distilled water, and agitate continuously for 2-3 hours using a magnetic stirrer to ensure uniform suspension. Carefully immerse calibrated pH and conductivity electrodes (figures II-6 and II-7) into the mixture without disturbing the stir bar. Record measurements every 4-6 minutes until three consecutive readings show ≤2% variation (±0.1 pH units for acidity, ±5 µS/cm for conductivity), indicating stabilization

Figure II-6: WTW Cond 3310 Portable Conductivity Meter

Figure II-7 :Consort C3030 Multi-Parameter Analyzer (pH Meter)

10. Determination of Sedimentation rate (APHA, 2017):

Sedimentation rate determination measures the settling velocity of suspended particles in a liquid medium under gravity. The principle is based on Stokes' law, where particles with higher density and larger size settle faster than lighter, smaller particles. By monitoring the interface between the clear supernatant and the sediment layer over time, the sedimentation rate can be quantified. This test is particularly useful for characterizing lime milk suspensions

- ***Pocedure :***

To determine the sedimentation rate, transfer 53 ml of well-mixed lime milk into a 100 ml test tube and place it upright. Observe and record the height of the water-mud interface every 3 minutes as the particles settle, noting the change in level over time (figure II-8).

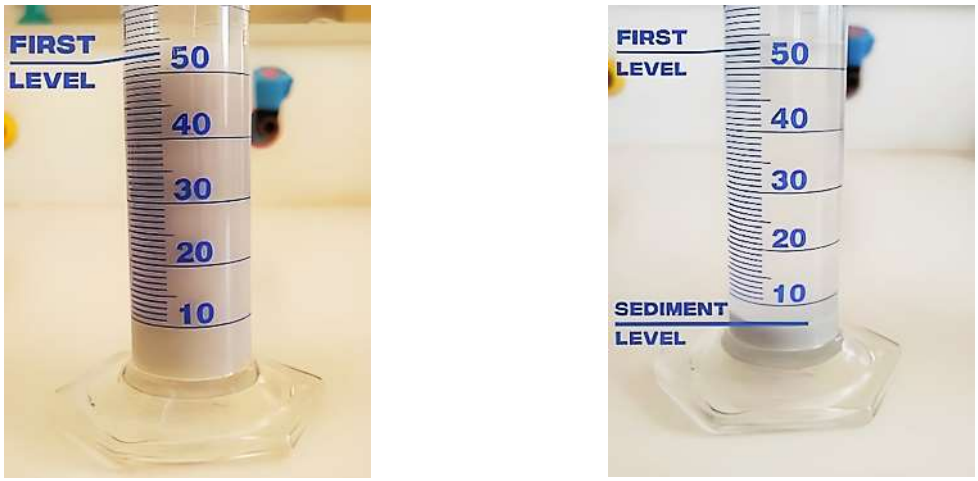

Sample at Initial Time **Sample After Sedimentation**

Figure II-8 :Sedimentation Process: Initial and Final Stages

11. Sulfate level (APHA, 2017):

This gravimetric method quantifies sulfate content through selective precipitation of barium sulfate ($BaSO_4$) under acidic conditions. The principle relies on the stoichiometric reaction between sulfate ions (SO_4^{2-}) and barium chloride ($BaCl_2$), forming an insoluble precipitate. By calcining the precipitate to remove organic residues and moisture, the remaining $BaSO_4$ mass provides a direct measure of sulfate content. The hydrochloric acid pretreatment eliminates interfering anions (e.g., carbonate, sulfite) and ensures complete dissolution of the sample.

- ***Procedure (figure II-9):***

1 g of the sample and 10 ml of 10% hydrochloric acid (HCl) are combined in a beaker. On a heated plate, the beaker is brought to a slow boil for ten minutes. The contents of the beaker are filtered into a flask after the boiling period has ended. To the filtrate, distilled water is added up to the 250ml mark. A beaker containing 100 milliliters of the filtrate is agitated vigorously. For ten minutes, the beaker is set on a heated pan. 10 ml of barium chloride ($BaCl_2$ 10%) is added to the contents of the beaker after the initial 8 minutes. The solution is filtered through paper once it has boiled. The contents of the filter paper are placed in a crucible for calcination in an oven at 900°C for 30 minutes.

Sulphate's content is expressed by:

$$\text{Sulfate content} = \frac{(P1\text{-}P2)}{P1} \textbf{ x 100.....(5)}$$

Where:

P1: Weight of crucible + filter paper.

P2: Weight of crucible after furnace calcination.

Slowly boiling

Weight of crucible+filter paper

Weight of crucible after furnace calcination

Crucible after furnace calcination

Figure II-9: Key Steps in Gravimetric Determination of Sulfate Content

12. Determination of carbonates rate (International Organization for Standardization. , 2014):

The determination of carbonate content is based on the calcimetric method, which measures the volume of carbon dioxide gas released when carbonates react with hydrochloric acid (HCl). The reaction follows the chemical equation:

$$CaCO_3 + 2HCl \rightarrow CaCl_2 + H_2O + CO_2\uparrow$$

The volume of CO_2 produced is directly proportional to the amount of carbonates present in the sample, allowing for quantitatie analysis through gas volumetry

- ***Procedure***

To determine the carbonate content of the sample, a test portion of 0.500 g previously dried at 105 °C is placed into the reaction flask of the CO_2-evolution apparatus (figure II.10). The flask is sealed and connected to the glass absorption tube and the calibrated gas-measurement burette. The upper reservoir is filled with standardized hydrochloric acid, and the stopcock is opened to allow the acid to flow by gravity into the reaction flask, where it reacts with the carbonates present in the sample

As the acid reacts with the carbonate, CO_2 gas is released, passes through the purification coil, and displaces the liquid in the graduated burette. Once the reaction is complete and no more gas is produced, the final displaced volume is recorded. In this test, the displaced volume corresponds to V_{HCl}, the volume of HCl equivalent to the gas produced.

Since the apparatus is calibrated such that V of displaced liquid corresponds to 0.500 g of $CaCO_3$, the carbonate mass is calculated by proportionality:

$$\mathbf{m_2 = (VHCl \times m_1) / V}\text{.....(1)}$$

Where

$\mathbf{m_2}$: mass of $CaCO_3$ in the sample

$\mathbf{m_1}$: initial dry mass of the sample

$\mathbf{V_{HCl}}$: the volume of HCl measured displaced volume (from the gas burette)

$\mathbf{m_1}$: initial dry mass of the sample

V : The calibration volume

The carbonate percentage is then expressed relative to the initial mass using

$$\mathbf{\%CaCO_3} = \frac{m_2}{m_1} \times \mathbf{100}\text{.....(2)}$$

Where

$\mathbf{m_1}$ = initial dry mass of the sample

$\mathbf{\%CaCO_3}$ = carbonate content of the sample

$\mathbf{m_2}$ = mass of $CaCO_3$

Figure II-10: Apparatus Setup for Determination of Carbonate Content by Calcimetric Method

13. Density measurement (ISO., 2016):

The density measurement after compaction method is based on volumetric analysis of bulk materials following controlled mechanical compaction. The sample is subjected to standardized compaction forces using a stampf volumeter, which applies consistent mechanical energy to eliminate air voids and achieve maximum packing density1. The final density is calculated by dividing the mass of the compacted sample by its final volume after compaction stabilizes

- ***Procedure :***

A 100 g sample of the material is placed into a graduated cylinder in the density tester (figure II-11). The cylinder is subjected to mechanical tapping for five minutes to compact the material. After tamping, the final volume of the sample is read directly from the cylinder scale.

The density after compaction is calculated using the formula:

$$\textbf{Density (g/cm}^3\textbf{) = m / V}\text{……..(6)}$$

Where

m = mass of the sample (g)

V = volume of the compacted sample (cm^3)

Figure II-11: STAV 2003 Stampf-volumeter

14. Porosity (Javadi & Zolfaghari, 2017):

Porosity quantifies the void fraction within a material, defined as the ratio of pore volume to total volume, expressed as a percentage. This method uses fluid displacement (e.g., methanol) to measure pore volume via saturation.

$$\textbf{Porosity (\%)} = (V_m / V_{app}) \times 100 \ldots\ldots (7)$$

Where

Vm: the methanol volume

Vapp**:** the apparent volume

15. Sulfur Removal (Ghosh & Chattopadhyay, 2008):

The removal of sulfur from the sample was conducted through a standardized chemical treatment process to ensure the elimination of sulfur compounds that could potentially influence the material's properties.

16. Washing with Distilled Water:

To remove soluble sulfur compounds such as calcium sulfide (CaS), the sieved powder is mixed with distilled water at a solid-to-liquid ratio of 1:5 and stirred for 30–60 minutes for proper dispersion. The mixture is then left to stand for 24 hours to allow sedimentation, after which the supernatant containing impurities is collected and the sediment discarded. This washing process is repeated 3–5 times until the pH stabilizes and the water remains clear. The final suspension is filtered, the residue is washed with distilled water, dried in an oven at 100 °C to constant weight, and, if needed, lightly ground to obtain a uniform powder.

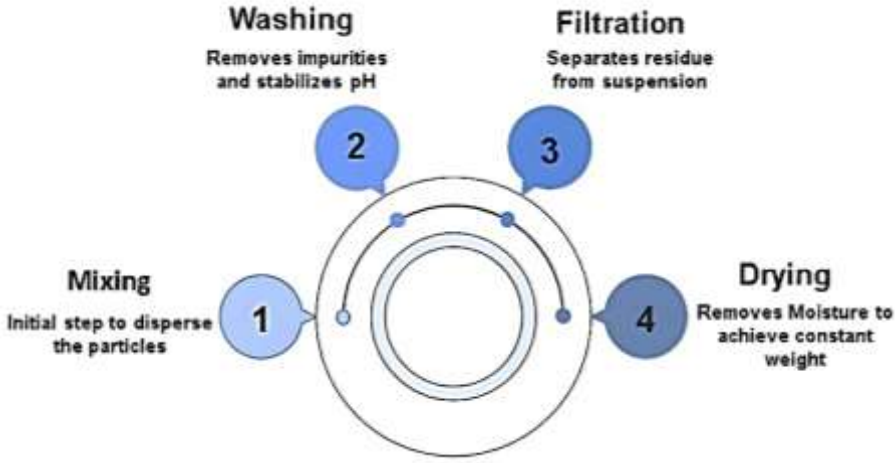

Figure II-12: Hydrated Lime Purification Process

17. Oxidation of Sulfur Compounds:

To convert sulfur impurities into stable sulfates, a 3–5% hydrogen peroxide (H_2O_2) solution is prepared and slowly added to the washed powder under continuous stirring. The required amount of H_2O_2 is calculated based on the sulfur content in the slag, following the stoichiometric ratio

$$S + 4H_2O_2 \rightarrow H_2SO_4 + 2H_2O,$$

where one mole of sulfur requires four moles of H_2O_2. The reaction is allowed to proceed for about two hours at room temperature, after which the solid residue is thoroughly washed with distilled water to remove the formed sulfates.

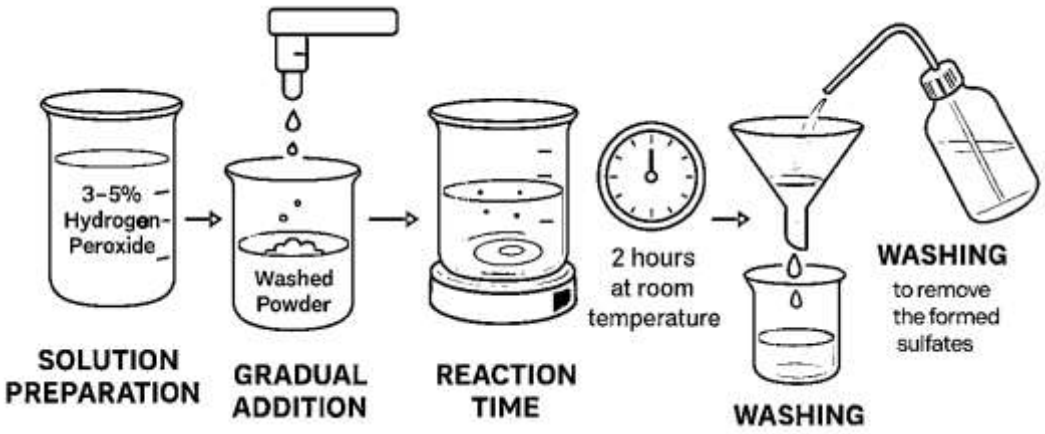

Figure II-13: Process for Converting Sulfur Impurities to Stable Sulfates

18. Drying and Calcination:

The oxidized material is first dried at 100 °C for 12 hours to remove moisture. It is then calcined at 750°C for 3 hours in air, a process that eliminates any residual sulfur and enhances the reactivity of the material.

References:

235-2001, N. (2001). *Ciments – Détermination de la perte au feu équivalente basée sur NE 2-1-008:1984*. Institut algérien de normalisation.

American Public Health Association (APHA), American Water Works Association (AWWA), & Water Environment Federation (WEF). (2017). *Standard methods for the examination of water and wastewater*. APHA.

ASTM International. (2018). *Standard test methods for sieve analysis of fine and coarse aggregates (C136/C136M)*. ASTM International.

Day, P. R. (1965). Particle fractionation and particle-size analysis. In *Methods of soil analysis* (Part 1, pp. 545–567). American Society of Agronomy; Soil Science Society of America.

Ghosh, S. K., & Chattopadhyay, B. (2008). Chemical treatment of soil for sulfur removal: A review. *Journal of Geotechnical and Environmental Engineering, 10*(2), 45–58.

Institut algérien de normalisation. (2014). *NA 5042: Liants – Bétons — Liants hydrauliques – Méthodes d'essais des ciments – Analyse chimique des ciments*. Adoptée le 13 novembre 2007, conforme à EN 196-2:2005. Catalogue des normes algériennes.

International Organization for Standardization. (2014). *ISO 10693:2014, Soil quality — Determination of carbonate content — Rapid titration method*. ISO.

ISO. (2016). *Geotechnical investigation and testing — Laboratory testing of soil — Part 4: Determination of dry density of soil samples (ISO 17892-4:2016)*. International Organization for Standardization.

Javadi, M., & Zolfaghari, M. (2017). Porosity measurement in porous materials: Methods and applications. *Materials Science and Engineering B, 212*, 74–80.

Latimer, G., Kane, P., Beine, R., Thiex, N., Raghe, H., Campbell, H., … Fitzloff, J. (2023). *Official methods of analysis of AOAC International*. AOAC Publications.

Chapter III : Linde Gas By product Characterization

Chapter III : Linde Gas By product Characterization

1. Introduction

This chapter details the characterization of carbide lime, a key raw material sourced from the acetylene gas industry (Linde Gas) in Sidi Bel Abbès. The following sections will cover the supplier's background and the physical and chemical properties of the collected materials

2. Raw Material: Carbide lime :

Carbide lime was used as a raw material in this work. It was collected from Linde Gas , the acetylene gas industry in Sidi Belabes (figure III-1).

Figure III-12:Aerial view of acetylene gas industry site located in Sidi Belabbes

3. Linde Gas production plant:

The Linde Gas production unit in Sidi Bel Abbès is located within the industrial zone of the city.

Linde Gas Sidi Bel Abbès produces a range of industrial and medical gases that serve various sectors. These include **Oxygen, Nitrogen, Argon, Nitrous Oxide** and **Compressed Air**. A key product of the site is **Acetylene (C_2H_2) gas**, which is primarily utilized in metal cutting, welding, and chemical synthesis.

Monthly, about 16 m^3 of water is injected throughout the production process, which uses about 4,200 kg of calcium carbide to generate 1,409 m^3 of acetylene gas. However, as a by-product, some 4,725 liters of hydrated lime slurry (lime milk) are also produced.

This slurry is from acetylene generation is pumped to a recessed-chamber filter press, where the slurry distributes across cloth-lined plates and pressure forces water through the cloth and internal ports while $Ca(OH)_2$ builds into a cake in each chamber, after the filtrate runs clear

and the cycle completes, the press is opened to discharge the dewatered carbide-lime cakes, which are then drained in the air.

4. Lime milk :

Lime milk sample was collected from the filtration unit within the lime milk waste processing area (figure III-2) using a clean, empty container . The sample was then transferred into a 5-liter plastic bottle for storage (figure III-3). The ambient temperature at the time of sampling was approximately 13 °C.

Figure III-2: The lime milk waste processing area

Figure III-3: Storage of Lime Milk Sample in 5-Liter Plastic Bottle

The physical properties are presented in table III-1

Table III-1: Physical Properties of lime milk

Material	Color	Odor	state at room temperature
lime milk	**light gray**	**chalky**	**milky-white liquid, showing visible sedimentation over time**

5. Lime milk characterization :

To understand its settling behavior, the rate of lime milk sedimentation was examined. This involved monitoring the change in lime milk volume over a specific time. The results are reported in figure III-4

The results indicate that the milk lime sedimentation occurs rapidly within 15min. So the short time sedimentation allows for a rapid and efficient recovery of the carbide lime.

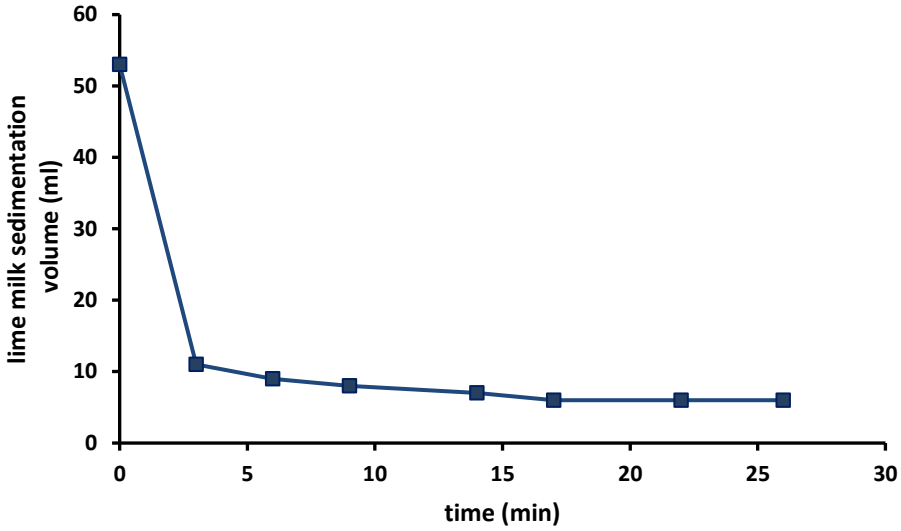

Figure III-4: Rate of lime milk sedimentation

6. Physicochemical characterization :

The lime milk exhibits a strongly alkaline character (table III-2). This result indicates the presence of free hydroxide ions. The electrical conductivity suggests a significant ionic content

Table III-2: Physicochemical properties of lime milk

Properties	pH	Conductivity (mS/cm)
Lime Milk	11.60	18.09

7. Carbide lime :

The sampling of carbide lime was conducted at the filtration unit of the lime milk waste processing area at the Linde Gas site. The lime milk first entered the filtration system (figure III-5), passing through several filters and undergoing pressure-based filtration (figure III-6). This process resulted in the separation of the solid carbide lime powder. after a clean shovel was used to collect the carbide lime (figure III-7), which was then placed into a clean, empty can for storage (figure III-7). The sample was taken during the same session as the lime milk

The carbide lime powder was distributed evenly on a large plastic sheet and left to dry under clear sunlight (figure III-8). The drying process took place over a period of approximately four days, with ambient temperatures averaging around 23°C

Figure III-5 : The filtration system

Figure III-6 : Filter Plate and Pressure-Based Filtration System

Figure III-7: Collection and Storage of Carbide Lime Powder

Figure III-8 : Drying of Carbide Lime Powder Under Sunlight

8. Carbide lime Characterization:

8.1 Physical properties :

The physical properties are presented in table III-3

Table III-3*:* Physical Properties of dry Carbide lime :

Material	Colour	odor	state at room temperature
Carbide lime	**grayish**	**Faint chalky**	**solid (a fine powder)**

The physicochemical properties of dry carbide lime were determined. This involved noting its appearance and state (figure III-7), as well as measuring key parameters like density and porosity, as detailed in the table III-4 :

Table III-4: Density and Porosity of Carbide Lime :

Properties	Density (g/cm^3)	Porosity (%)
Carbide lime	0.833	77.5

The physical properties of raw materials (high porosity and low bulk density), play a crucial role in determining the efficiency and quality of hydroxyapatite (HAp) synthesis. Such characteristics are commonly observed in biogenic wastes like fish bones, eggshells, and certain plant-derived materials. High porosity enhances the reactive surface area (Mondal, Mondal, Dey, & Mukhopadhyay, 2012); low bulk density generally corresponds to a light, open microstructure, which can aid in thermal decomposition and subsequent reaction with phosphate sources (Kareem & Eyiler, 2024). Also, the physical characteristics of the raw materials influence the functional quality of the final HAp product (Prakasam, et al., 2015).

8.2 pH evolution :

Table III-5: Variation of carbid lime pH over Time

T(min)	0	4	8	13	17	21	27	35	44	55	64	74
pH	11.24	11.39	11.44	11.48	11.51	11.53	11.55	11.55	11.54	11.53	11.52	11.52

The carbide lime solution quickly reaches a stable pH, indicating chemical equilibrium, with slight variations likely due to CO_2 absorption from the air. Although lime milk maintains a slightly higher pH (11.60) than the carbide lime solution (11.52-11.55), this difference may result from higher saturation and reduced CO_2 interaction (Han, Yoo, Kim, & Wee, 2011)

8.3 Chemical properties :

The chemical composition of the carbide lime was measured by XRF and data are tabulated in Table III-6

Table III-6: Chemical Composition of Carbide Lime by Oxides (%)

oxide	CaO	SiO_2	Al_2O_3	Fe_2O_3	SO_3	Cl	MgO	K_2O	Na_2O
carbide lime (%)	65.65	3.175	1.177	0.125	0.537	0.08	0.299	0.266	0.004

The carbide lime is composed of calcium oxide (CaO) of 65.65% and SO_3 (0.537%) and other oxide compounds such as MgO, Na_2O, K_2O and SiO_2. The calcium carbonate ($CaCO_3$) content in carbide lime is estimated to 23% (table III-7). These results suggest the suitability of the sample as a calcium precursor for hydroxyapatite synthesis.

Table III-7: Chemical properties of Carbide Lime Residue

Properties	pH	Conductivity (mS/cm)	Humidity (%)	sulfates (%)	$CaCO_3$ (%)	LOI
Carbide lime	11.52	11.62	25	0.73	23	28.61

8.4 Granulometric analysis :

To assess the particle size distribution of the carbide lime, a sieve analysis was performed using mesh sizes ranging from 106 µm to 53 µm. The results, illustrated in Figure III-9, show that the largest fraction of the sample (55%) was retained on the 106 µm sieve. In contrast, only 6% were retained on the 53 µm sieve while 12% of the material passed through all sieves and was collected

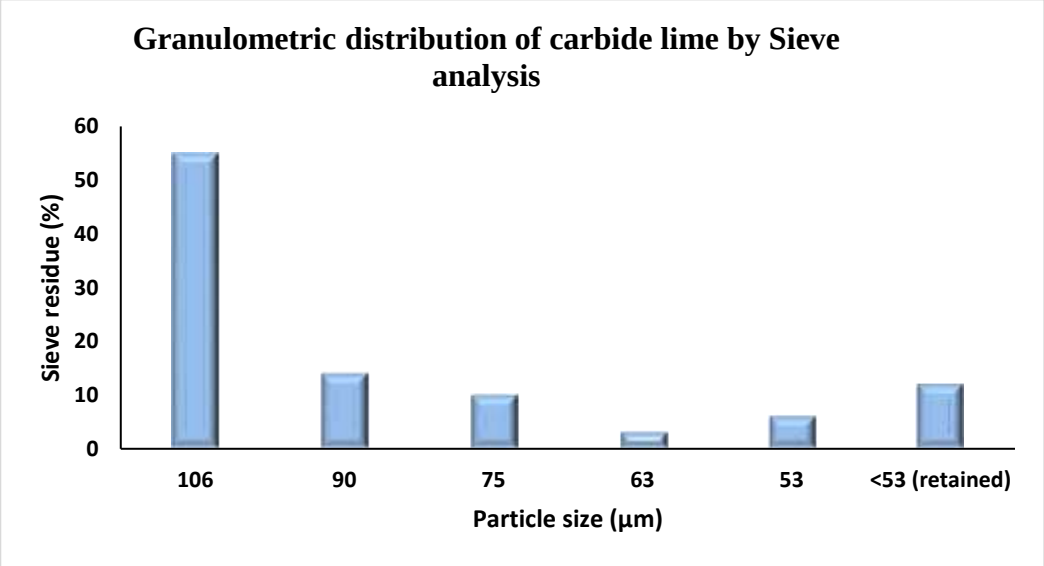

Figure III-9: Particle Size Distribution of Carbide Lime by Sieve analysis (106µm to 53µm)

as fine residue. This dominance of coarse particles confirms a relatively broad but skewed granulometric distribution, which may significantly influence the sample's solubility, filtration behavior, and reactivity during hydroxyapatite synthesis (Hossain, et al., 2021).

8.5 Carbide lime FTIR Spectral :

The Figure III-10 determines the functional groups in carbide lime. The strong absorption band observed at approximately 1400 cm^{-1} and the weak band at 2508 cm^{-1} (carbonate groups CO_3^{2-}), confirming partial carbonation of $Ca(OH)_2$ due to exposure to atmospheric CO_2 (Cizer, et al., 2012).

The strong O–H stretching band at 3643 cm^{-1} and the H–O–H bending vibration at 1580 cm^{-1} are due to the presence of $Ca(OH)_2$ which is only present in lime hydrate (Vu, et al., 2019).

The characteristic band of calcite 873 cm^{-1} (O–C–O) is appeared (Taylor, et al., 1995) . The figure demonstrates the presence of the characteristic absorption band of amorphous carbonate calcite at ~1070 cm^{-1}. It can be attributed to the symmetric C–O stretch in non-Centro symmetric structures (Farmer , 1974).

The wide band peak approximately at 530 cm^{-1} illustrates the presence of Ca–O band of symmetric vibration (Siriprom, Teanchai , Kirdsiri, & Kaewkhao, 2014).

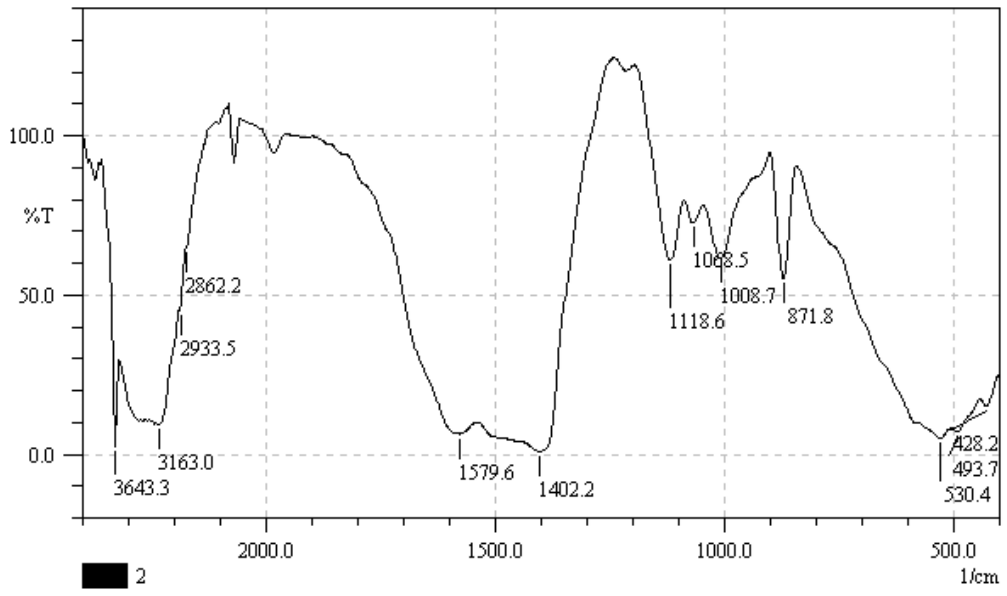

Figure III-10: FTIR carbide lime Spectra

8.6 EDS analysis :

Energy Dispersive X-ray Spectroscopy (EDS) analysis was performed to qualitatively assess the elemental composition of the hydrated lime sample. The spectrum (figure III-11) revealed a predominant presence of calcium (95.29%), consistent with the expected major component of $Ca(OH)_2$. Minor signals corresponding to elements such as silicon (Si), aluminum (Al), iron

(Fe), manganese (Mn), and strontium (Sr) were also detected, suggesting the presence of naturally occurring mineral impurities derived from the raw material.

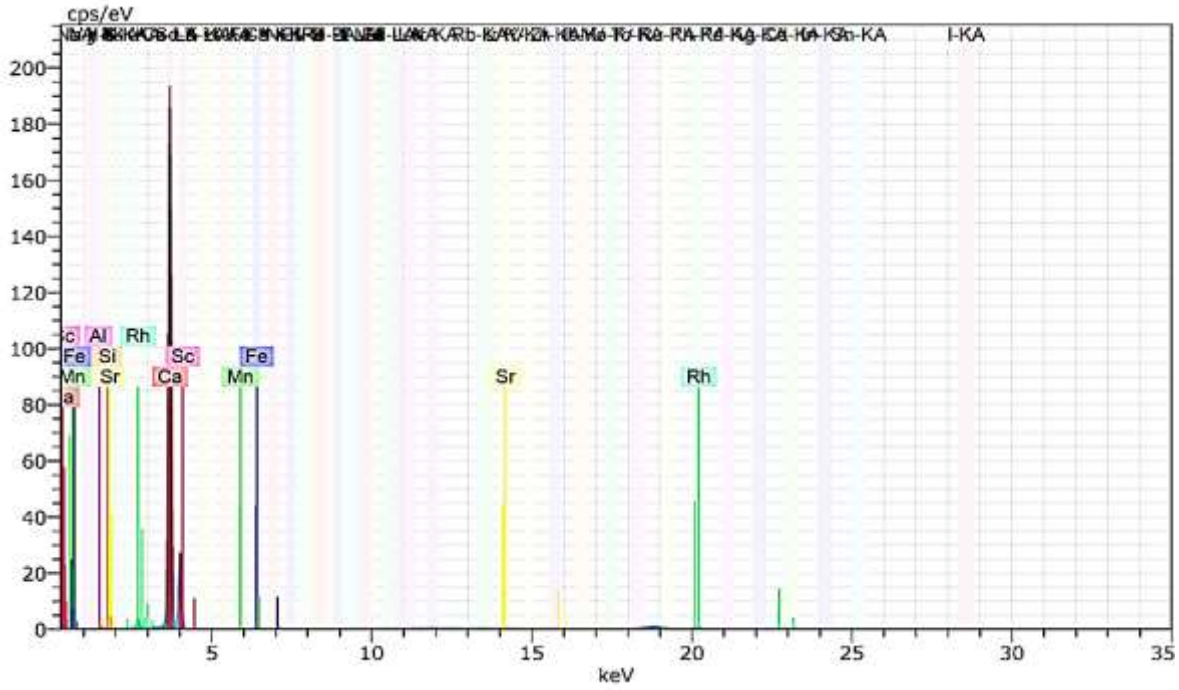

Element	%
Al	0.48
Si	1.11
Ca	95.29
Sc	0.01
Mn	0.01
Fe	0.17
Sr	0.09
Rh	2.86

Its elemental composition is shown in the inset table.

Figure III-11: EDS spectrum of Linde Gas by product .

8.7 XRD analysis :

X-ray diffractogram of the industrial by product (Figure III-12) indicates predominance of calcium hydroxide and minor presence of carbonate. The major diffraction peaks at 2θ = 17.9°, 34° and 50°correspond to portlandite in good agreement with JCPDS (N°.file number 01–087–0673) card (Delhomme, et al., 2022).. In addition, the peak at 2θ = 29.2°, suggests the possible presence of calcite, which may be attributed to partial carbonation during material handling or exposure to atmospheric CO_2 (Nurfiana, Kadarwati, & Putra, 2020).

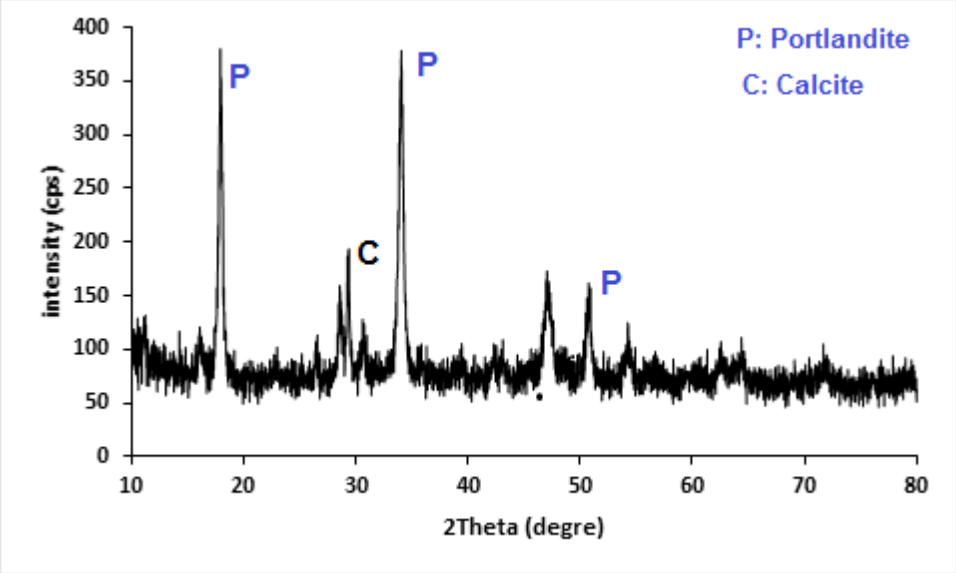

Figure III-12 : X-ray diffractogramm of the Industrial by product

9. Conclusion :

The carbide lime by-product from the acetylene industry Linde Gas Sidi Bel Abbès is a potential precursor for hydroxyapatite synthesis. The by-product is predominantly composed of calcium hydroxide. Physicochemical characterization revealed its strongly alkaline nature, high porosity, and low bulk density. These properties enhance reactivity and favor subsequent transformation processes. Also the granulometric distribution supports its potential by providing a reactive surface area. These results establish carbide lime not only as a waste stream requiring valorization but also as a promising, low-cost, and sustainable calcium source for Hydroxyapatite synthesis. Furthermore, this study aligns with both circular economy and environmental management strategies.

References:

Adnen, N. A., Halim, N. A., & Nor, M. A. (2017, September). Development of hydroxyapatite from Setiu coral via hydrothermal method. In *AIP Conference Proceedings, 1885*. AIP Publishing.

Cizer, Ö., Rodriguez-Navarro, C., Ruiz-Agudo, E., Elsen, J., Van Gemert, D., & Van Balen, K. (2012). Phase and morphology evolution of calcium carbonate precipitated by carbonation of hydrated lime. *Journal of Materials Science, 47*(16), 6151–6165.

Delhomme, F., Prud'homme, E., Julliot, C., Guillot, T., Amziane, S., & Marceaux, S. (2022). Effect of hemp on cement hydration: Experimental characterization of the interfacial transition zone. *Results in Chemistry, 4*, 100440.

Farmer, V. C. (Ed.). (1974). *The infrared spectra of minerals* (Vol. 4). London: Mineralogical Society.

Han, S. J., Yoo, M., Kim, D. W., & Wee, J. H. (2011). Carbon dioxide capture using calcium hydroxide aqueous solution as the absorbent. *Energy & Fuels, 25*(8), 3825–3834.

Hossain, M. S., Mahmud, M., Sultana, S., Bin Mobarak, M., Islam, M. S., & Ahmed, S. (2021). Coupled effect of particle size of the source materials and calcination temperature on the direct synthesis of hydroxyapatite. *Royal Society Open Science, 8*(9), 210684.

Kareem, Z., & Eyiler, E. (2024). Synthesis of hydroxyapatite from eggshells via wet chemical precipitation: A review. *RSC Advances, 14*(30), 21439–21452.

Mondal, S., Mondal, B., Dey, A., & Mukhopadhyay, S. (2012). Studies on processing and characterization of hydroxyapatite biomaterials from different biowastes. *Journal of Minerals & Materials Characterization and Engineering, 11*(1), 55–67.

Nurfiana, F., Kadarwati, A., & Putra, S. (2020). Synthesis and characterization of hydroxyapatite from duck eggshell modified silver by gamma radiolysis method. *Journal of Physics: Conference Series, 1436*(1), 012099.

Prakasam, M., Locs, J., Salma-Ancane, K., Loca, D., Largeteau, A., & Berzina-Cimdina, L. (2015). Fabrication, properties and applications of dense hydroxyapatite: A review. *Journal of Functional Biomaterials, 6*(4), 1099–1140.

Siriprom, W., Teanchai, K., Kirdsiri, K., & Kaewkhao, J. (2014). Characterization of calcium hydroxide derived from waste eggshell upon moisture effect. *Advanced Materials Research, 979*, 435–439.

Taylor, D. R., Crowther, R. S., Cozart, J. C., Sharrock, P. D., Wu, J., & Soloway, R. (1995). Calcium carbonate in cholesterol gallstones: Polymorphism, distribution, and hypotheses about pathogenesis. *Hepatology, 22*(2), 488–496.

Vu, H. H., Khan, M. D., Chilakala, R., Lai, T., Thenepalli, T., Ahn, J. W., & Kim, J. (2019). Utilization of lime mud waste from paper mills for efficient phosphorus removal. *Sustainability, 11*(6), 1524.

Chapter IV : Production of a hydroxyapatite-based ceramic for dental coating

Chapter IV : Production of a hydroxyapatite-based ceramic for dental coating

1. Introduction :

In the present chapter, we propose the carbide lime as an eco-friendly calcium source to hydroxyapatite (HAp) synthesis. The synthesis was carried out using a wet chemical method under ambient conditions is choosed for the synthesis. The obtained Hap was subsequently, characterized by FTIR spectroscopy and XRay Diffraction. Furthermore, zinc was incorporated as a dopant to enhance the biological performance of the material, with the objective of developing a bioactive ceramic suitable for dental implant coatings. The antimicrobial behavior of the Zn-doped HAp was also investigated to assess its potential in biomedical applications.

2. Hydroxyapatite Synthesis :

In the first stage of this study, hydroxyapatite (HAp) was synthesized using the wet chemical method with carbide lime as the calcium precursor. Different particle size fractions of the starting material were employed in order to evaluate their influence on the structural properties of the obtained HAp. This section presents the synthesis methodology in detail, along with the characterization techniques used to analyze the physicochemical and structural features of the synthesized powders.

3. The experimental procedure of HA Powder Synthesis via Wet Chemical Method :

The hydroxyapatite (HA) powder was synthetized according to a novel wet chemical method comprising precipitation from aqueous medium via a titration process by reacting calcium ion with phosphate ion based on a molar ratio of Ca/P = 1.67 and maintained in basic range at a pH around 10 (Rodríguez-Lugo, et al., 2018). The starting precursors used were carbide slag pretreated as calcium source and ammonium phosphate [$(NH_4)_2HPO_4$] (99.0% purity, Panreac (Monplet & Esteban S.A) following the chemical reaction:

$$\mathbf{10\ Ca(OH)_2 + 6H_3PO_4 \Rightarrow Ca_{10}(PO_4)_6(OH)_2 + 18\ H_2O\ldots\ldots\ (1)}$$

So this synthesis process involved the preparation of H_3PO_4 and $Ca(OH)_2$ solutions.

3.1 Preparation of $Ca(OH)_2$ solution (*Solution A*) :

The preparation of $Ca(OH)_2$ solution starts firstly by carbide slag treatment.

3.1.1 Treatment of the carbide slag :

The waste was treated by the following methods;

The slag is dried at 100°C in oven for 24h. The dried slag was ground by mortar, and sieved to obtain a fine homogeneous powder (45µm-180µm).

The following step is to remove sulfur traces. These traces can affect solubility, setting kinetics, and biocompatibility of the biomaterial (ISO, B.13779-2, 2000), and thus ensure the production of high-purity hydroxyapatite suitable for biomedical applications.

For that, the dried powder is washed with distilled water (solid-to-liquid ratio 1:5). stirred for 30–60 min, then left to stand for 24 h the supernatant is collected and the sediment discarded, and this washing step is repeated 3–5 times with fresh distilled water until the pH stabilizes and the water remains clear. The final suspension is filtered through filter paper or a Büchner funnel, the solid residue is rinsed with distilled water, dried in an oven at 75 °C until constant weight, and lightly ground to obtain a homogeneous powder. Subsequently, a 3% hydrogen peroxide (H_2O_2) solution is prepared and slowly added to the washed slag under constant stirring for about 2 h to oxidize sulfur-containing species into sulfates, according to the reaction

$$\mathbf{S + 4H_2O_2 \rightarrow H_2SO_4 + 2H_2O}\text{……..(2)}$$

Finally, the solid is washed again with distilled water to remove the sulfates formed

After which the residue is thoroughly washed. The washed material is dried at 100 °C and then calcined at 750°C for 3 hours to eliminate residual sulfur and improve reactivity.

Subsequently, the powder was sieved through a stack of wire mesh sieves with mesh sizes of: 45µm, 75µm and 106 µm to obtain distinct particle fractions. This process also facilitated the breakdown of agglomerates. Each particle fraction was then dispersed in water to prepare a calcium solution (*solution A*).

3.2 Preparation of Acidic solution (*Solution B*):

To prepare the H_3PO_4 solution (*Solution B*), the required amount of H_3PO_4 was diluted in distilled water, stirred for 10 minutes and subsequently contained in a titration funnel.

3.3 Hap Synthesis (figure IV-1) :

The phosphate solution (*solution A*) is added dropwise into the calcium solution (*solution B*) under stirring at 39°C for 20 min. The carbide-lime precursor produced a highly alkaline environment, therefore the pH was maintained around 10 by the addition of small amounts of

chloride acid (HCl) solution (37% concentration). The mixture is strirred for 5h. The mixture is left for 24 hours to ensure complete precipitation. Finally, the product is filtered, washed and dried at 100°C for 24h The dried powder is calcined at 750 °C for 2 hours to enhance crystallinity and physical properties (Hossain, et al., 2021).

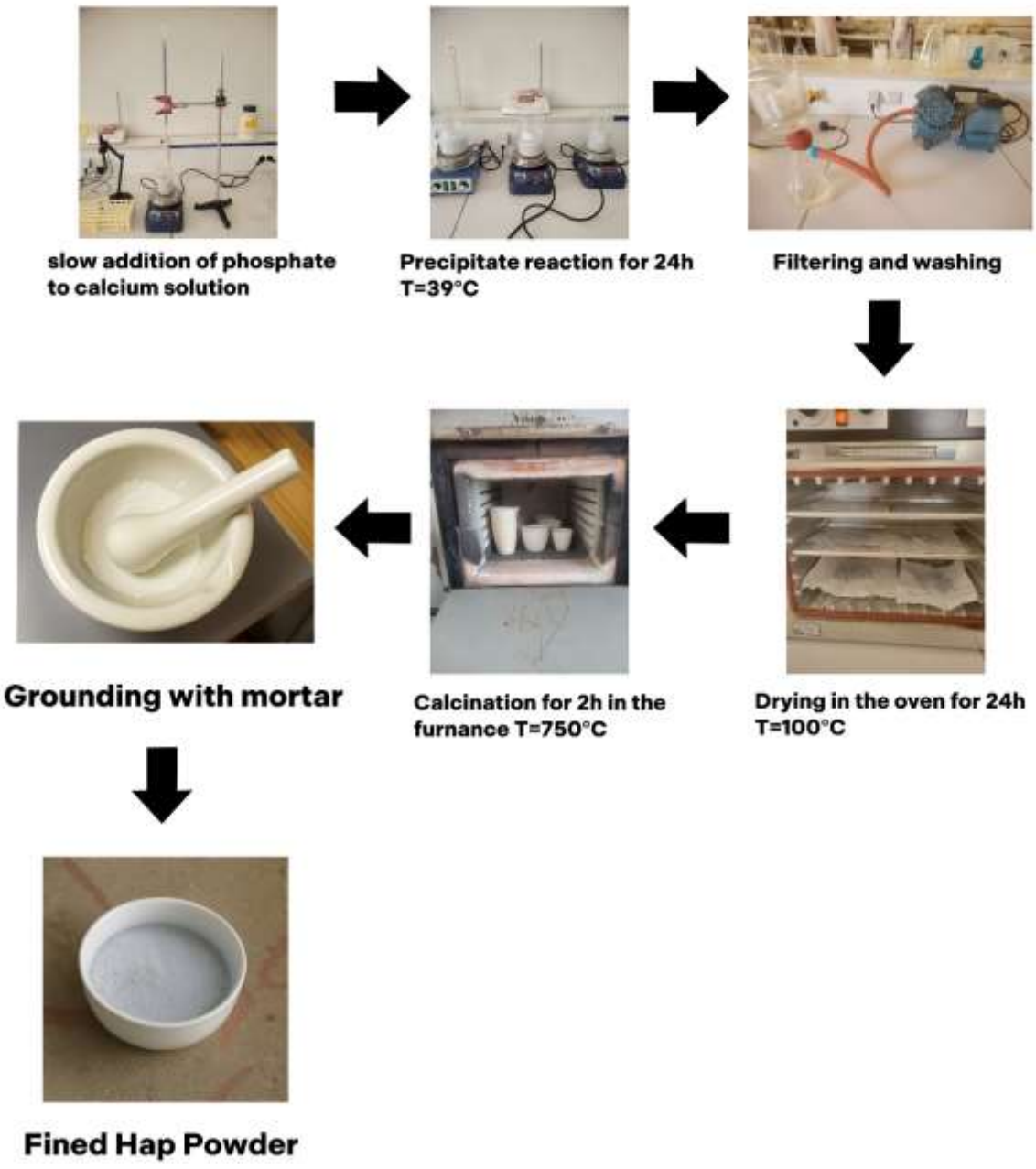

Figure IV-1 .: Hap Synthesis procedure

4. Characterization of the synthetized Hap :

4.1 Fourier transform infrared spectrophotometer: molecular structure investigation:

The FTIR spectra acquired for synthesized n-HAps are shown in Figure **IV-2** Observed data revealed the presence of the characteristic FT-IR band positions for PO_4^{-3} group, which are in

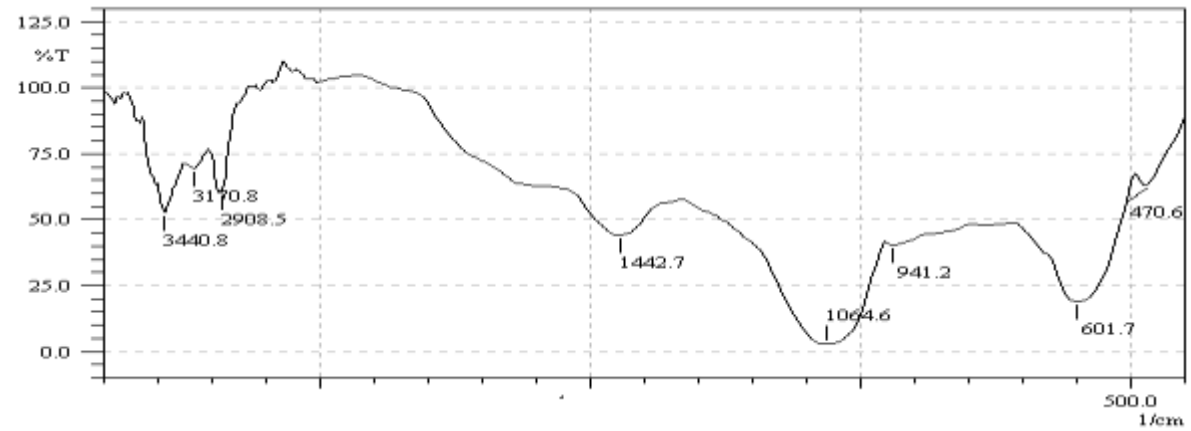

45-Hap

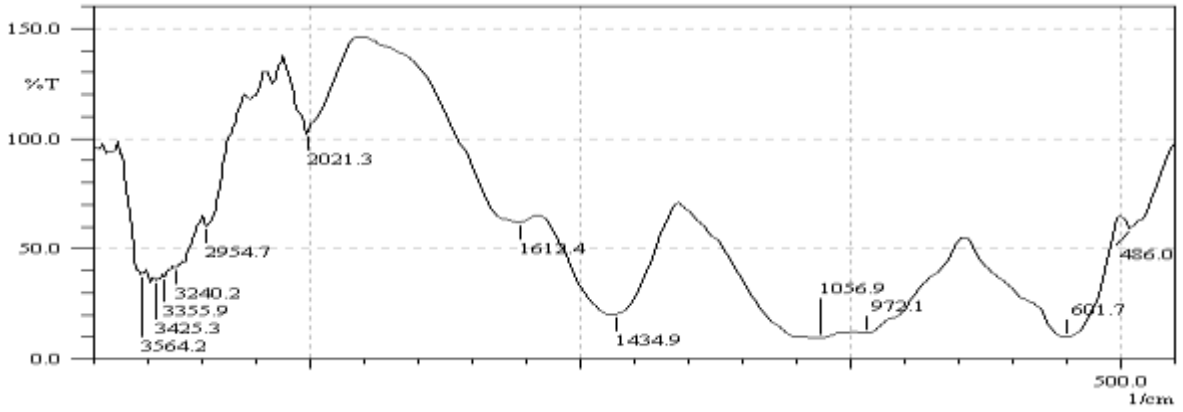

75-Hap

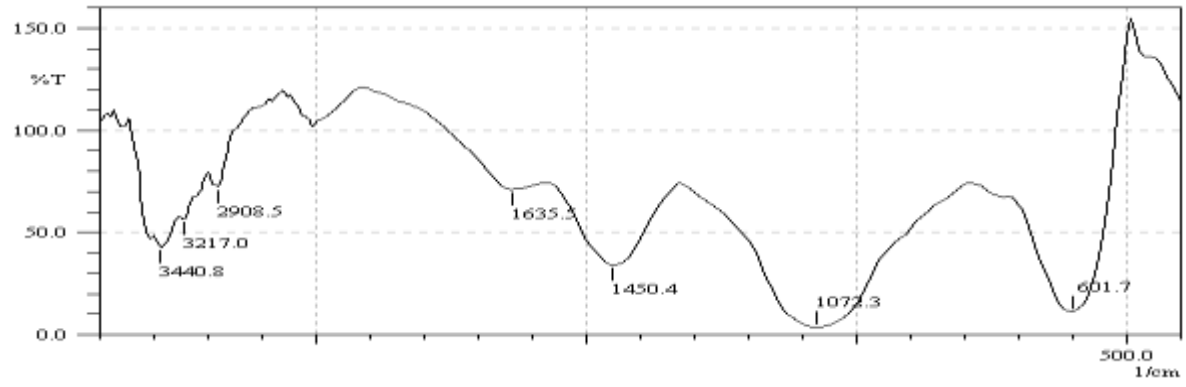

106-Hap

Figure IV-2 : FTIR spectrum of synthetized Hydroxyapatites

well agreement with previous studies (Senthilkumar, Dhivya, Sathya, & Rajendran, 2021). The 45-HAp sample exhibited various significant bands for the phosphate anions (PO_4^{-3}) along with some other bands in the range of 400–4000 cm^{-1}. The significant characteristic band at 1064 cm^{-1} corresponds to ν_3 (asymmetric stretching mode of P-O). It is one of the fundamental vibrational modes of the phosphate and confirms the formation of Hap in the current sample (Gopi, Indira, Kavitha , Sekar, & Mudali, 2012) (Michael, et al., 2016). Other PO_4^{-3} bands were observed at 470 cm^{-1} corresponding to ν_2 (symmetric bending mode of O-P-O) and 941 cm^{-1} corresponding to υ1 (symmetric stretching mode of P-O) while 603 cm^{-1} corresponds to PO_4^{-3} with ν4 (asymmetric bending mode of O-P-O) (Fleet, Liu, & King, 2004).

A small fraction of carbide slag powder reacted with the atmospheric carbon dioxide, resulting in the presence of carbonate anions ($CO3^{-2}$) revealed by the band at 1442 cm^{-1} (Kothari, et al., 2024). The tiny bands showed up at 1639 cm^{-1} and around 3568–3900 cm^{-1} because of the hydroxyl group (OH) bending and stretching vibrations, respectively. The bands at 2900 cm^{-1} indicated the presence of CO_2 that can be absorbed from the atmosphere (Bandyopadhyay, Mitra, Goodman, Kumar, & Bose, 2023).

5. X-ray Diffraction: mineral structure investigation

The acquired X-ray diffractograms for synthesized Hap samples using different sizes of carbide slag particle are shown in Figure IV-3 The thermal calcination at 850°C for HAp synthesis was sufficient to obtain a crystalline structure. The patterns exhibited a major intense peak for HAp at 2θ value of 32.1°. Other secondary peaks for HAp were present at 2θ values of 25.9°◦ with some less intense peaks at 2θ values of 28.1° and 29° (Rajesh, Hariharasubramanian, & Ravichandra, 2012). Some minor peaks corresponding to calcite were also identified at 2θ values of 21° and 23.1° (Mao, Liu, Zhang, & Li, 2020) (Guo, et al., 2017). So, the XRD patterns verified the successful synthesis of HAp with a trace amount of $CaCO_3$.

The Hap samples (45-Hap and 75-Hap) synthesized using smaller particle sized starting materials exhibited a reduced amount of crystallinity, while this value was comparatively higher for Hap samples prepared from larger sized materials (106-Hap).

The sample prepared from the 106µm precursor displays the sharpest and most intense diffraction peaks, particularly at the reflection near $2\theta \approx 32.1°$, indicating a higher degree of crystallinity and larger coherent crystalline domains. The relatively low background intensity in this pattern further confirms a reduced amorphous fraction, in contrast with the other samples.

The 75µm sample exhibits an intermediate behavior, with distinct HAp reflections but also minor secondary peaks around $2\theta \approx 21–23°$, corresponding to traces of calcite ($CaCO_3$). This indicates that the conversion of the precursor was not entirely complete in some regions.

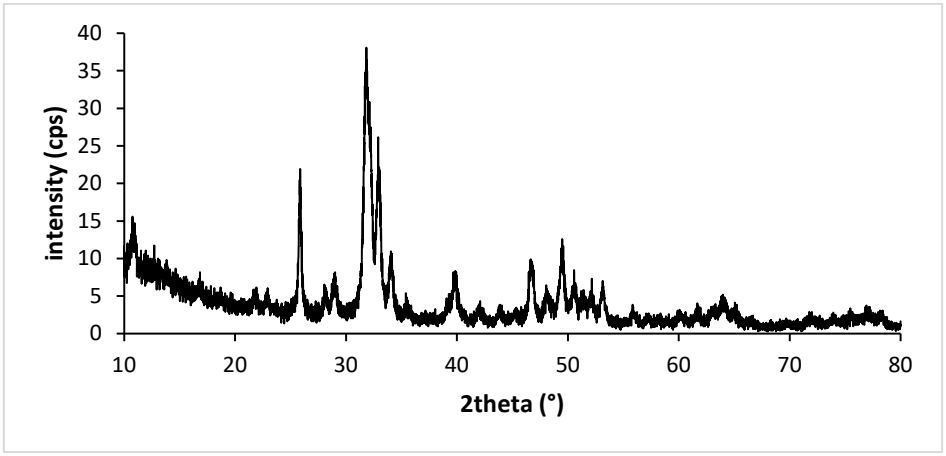

106-Hap

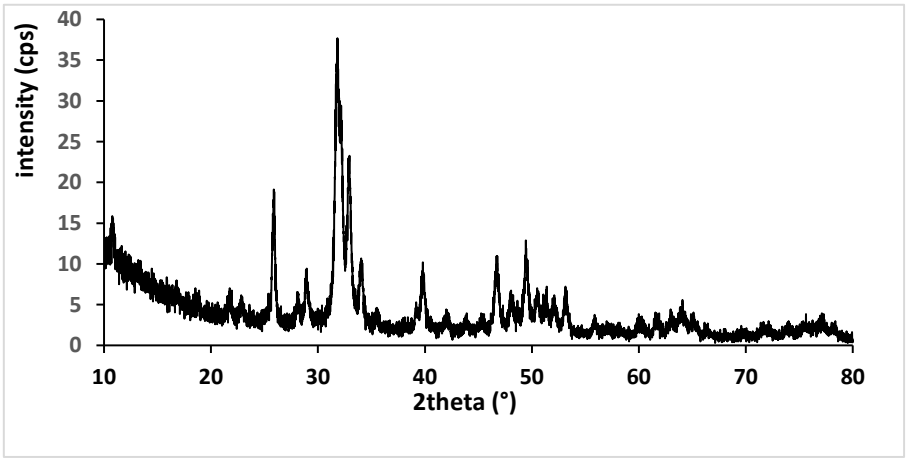

75-Hap

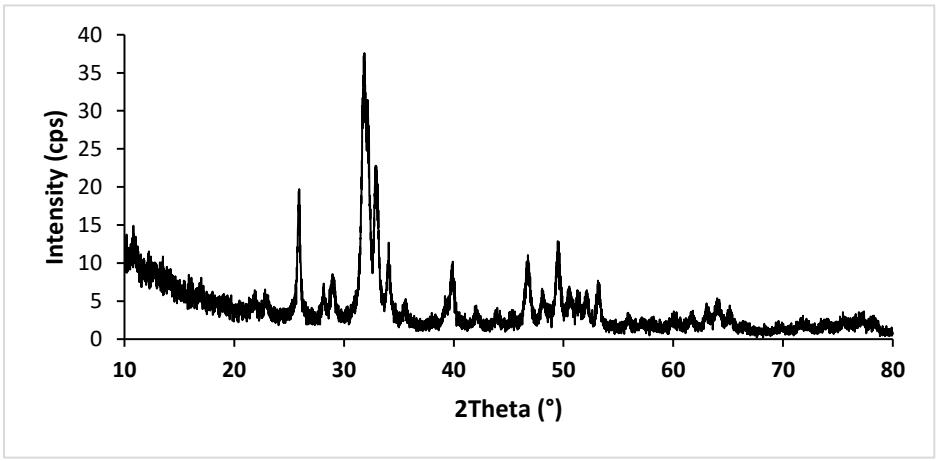

45-Hap

Figure IV-3 : XRD diffractograms of synthetized Haps

These findings reveal that the particle size of the carbide slag precursor significantly affects the crystal growth and phase purity of the resulting HAp. Larger precursor particles (106 µm) promote the formation of highly ordered and well-crystallized HAp structures, whereas smaller fractions favor the formation of less crystalline or partially amorphous apatite.

From an application perspective, a highly crystalline HAp coating (as obtained from the 106 µm precursor) is more desirable for bioceramic coating purposes.

6. Zn-doped Hydroxyapatite synthesis :

The present protocol outlines the zinc doping of hydroxyapatite (HAp) using zinc acetate or zinc nitrate as precursor salts, followed by a controlled calcination process. The synthesis strategy integrates mechanochemical activation to facilitate the uniform incorporation of Zn^{2+} ions into the HAp crystal lattice. This approach is intended to enhance the bioactivity and antibacterial performance of the material while maintaining its structural integrity and thermal stability.

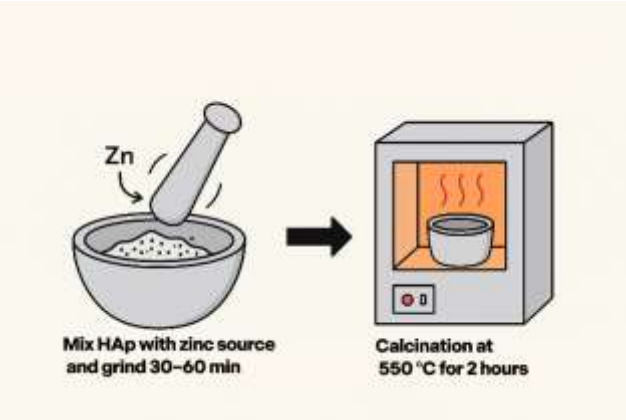

Figure IV-4 : Zn-Doped Hydroxyapatite synthesis procedure

7. Characterization of the synthetized Zn-Hap

7.1 Fourier transform infrared spectrophotometer: molecular structure investigation:

The FTIR spectrum acquired for Zn-nHap, are shown in figure **IV-2** The same PO_4^{3-} functional groups characteristic of the apatite phase are still present in all Zn–HAp samples.. The FTIR spectrum of the Zn-doped hydroxyapatite exhibits the characteristic vibrational modes of phosphate groups (PO_4^{3-}) at approximately 1049, 586, and 486 cm^{-1}, along with the typical hydroxyl (OH^-) stretching and adsorbed water bending bands appearing in the 3470–3300 cm^{-1}

and 1628 cm^{-1} regions, respectively. In comparison with un-doped HAp, these absorption bands display slight broadening and subtle shifts toward lower wavenumbers, reflecting lattice perturbations and local structural distortions induced by the partial substitution of Ca^{2+} with Zn^{2+} ions. These spectral modifications provide strong evidence of the effective incorporation of Zn^{2+} into the hydroxyapatite lattice, which consequently results in a slightly disordered and less symmetric phosphate environment, consistent with previous reports on Zn-doped apatites. The PO_4^{3-} bands observed around 1044 cm^{-1} on 106-Hap have merged into a broad band centered at approximately 1049.2 cm^{-1} for the Zn-106Hap as it observed in figure **IV-5** A broad band located at 3500 cm^{-1} is attributed to water molecules adsorbed on the surface of the Zn–106HAp crystals. However FTIR spectra of all three samples revealed a decrease of the peak intensities when the zinc is incorporated. This behavior suggests a decrease of the sample crystallinities with the introdduction of zinc content (Popa, et al., 2016)

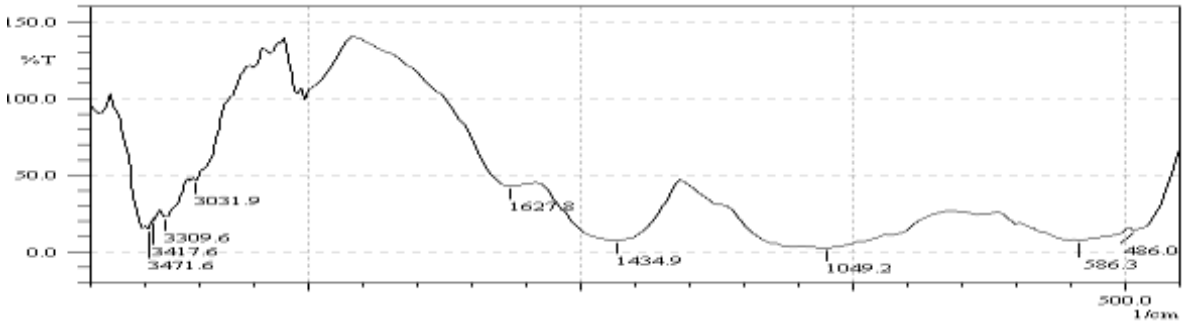

Figure IV-5 : FTIR spectrum of ZnA-106Hap

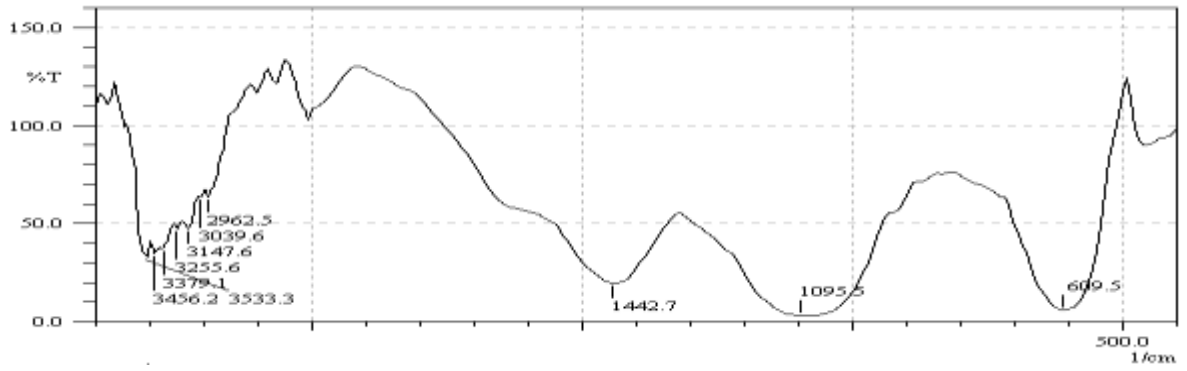

Figure IV-6 : FTIR spectrum of ZnN-75Hap

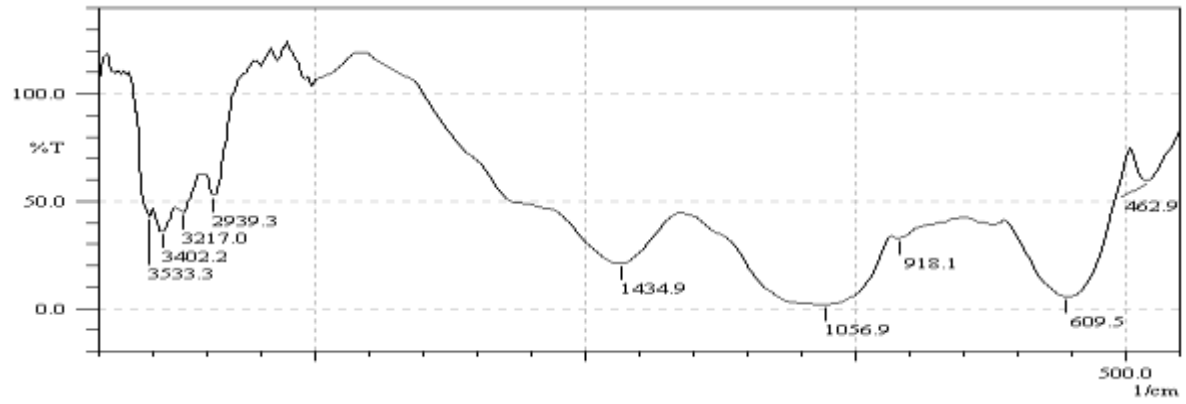

Figure IV-7 : FTIR spectrum of ZnA-45Hap

7.2 X-ray Diffraction: mineral structure investigation :

The X-ray diffraction patterns of hydroxyapatite doped with Zn (Zn-Haps) are presented in Figure IV-8

The characteristic peaks of hydroxyapatite (HAp) were detected in all the Zn-Haps, indicating the preservation of its apatite structure following the substitution operations. No additional peaks related to secondary phases are detected, confirming the successful substitution of Zn^{2+} ions within the apatite lattice without altering its structure.

A slight variation in peak intensity and broadening is observed with the particle size. The sample with the smallest particle size (ZnA-45HAp) exhibits broader peaks and lower intensity, indicating reduced crystallinity and smaller coherent domain size (Li , Xiao, Liu, Chen, & Huang, 2008). Conversely, the ZnA-106HAp sample presents sharper and more intense reflections, characteristic of higher crystallinity and larger crystallite domains (Hossain, et al., Coupled effect of particle size of the source materials and calcination temperature on the direct synthesis of hydroxyapatite. , 2021). The use of zinc acetate tends to favor better structural ordering and higher crystallinity, while zinc nitrate precursors yield slightly more defective or nanocrystalline apatite structures.

A slight variation in peak intensity and broadening is observed with the particle size. The sample with the smallest particle size (ZnA-45HAp) exhibits broader peaks and lower intensity, indicating reduced crystallinity and smaller coherent domain size (Ren, Xin, Ge, & Leng, 2009). Conversely, the ZnA-106HAp sample presents sharper and more intense reflections, characteristic of higher crystallinity and larger crystallite domains.

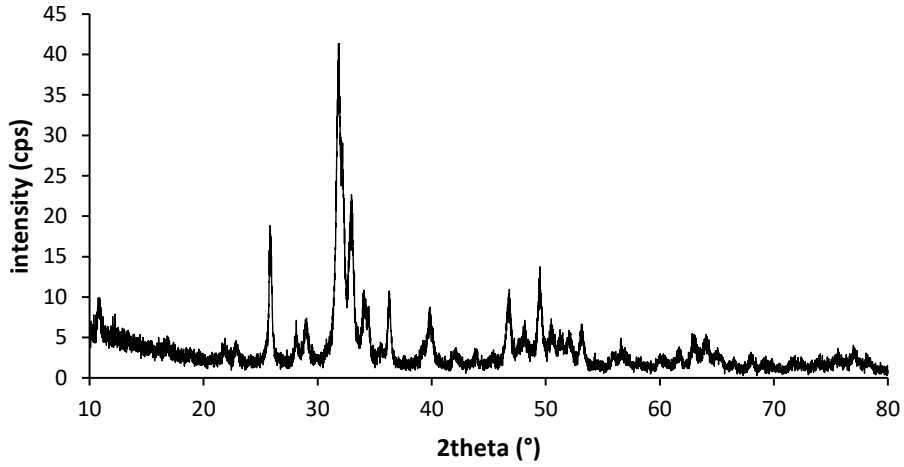

ZnA-106Hap

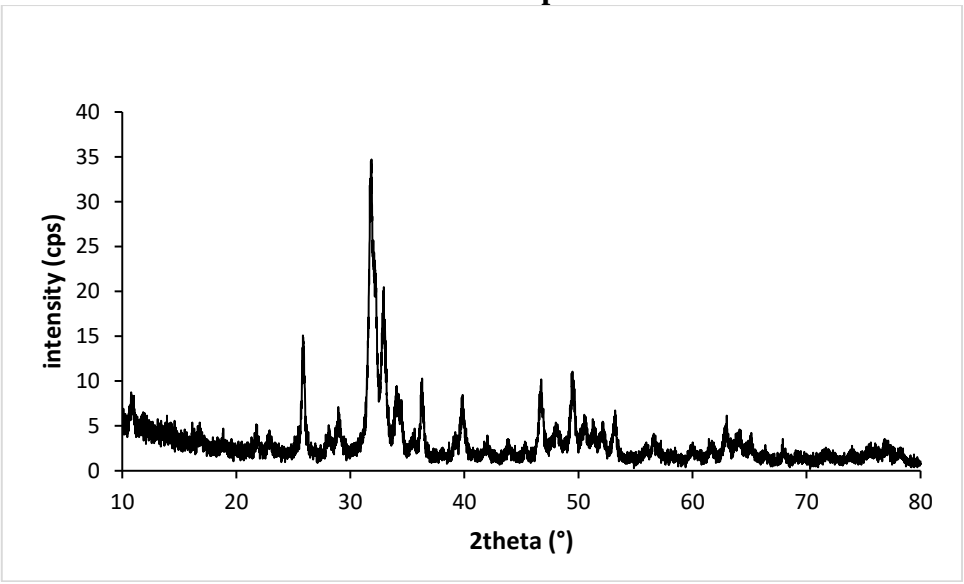

ZnA-45Hap

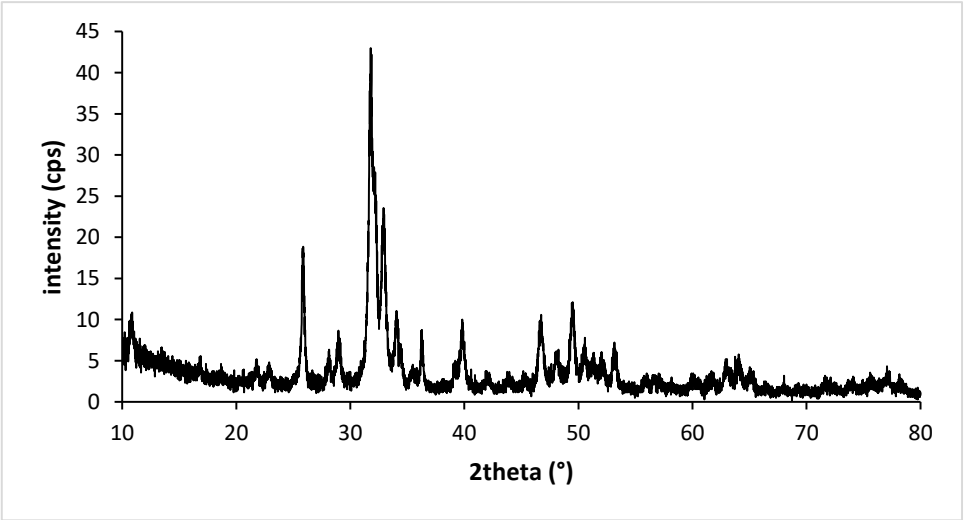

ZnN-75Hap

Figure IV-8 : XRD diffractograms of synthetized Zn-Haps

8. Antibacterial effect of Zn doped hydroxyapatite :

8.1 Principle :

The purpose of this protocol is to isolate bacterial strains naturally present in the human oral for use as test organisms in evaluating the antibacterial activity of a given material. Saliva, as a representative biological fluid, contains a variety of oral microorganisms including both aerobic and facultative anaerobic bacteria (Troeltzsch, et al., 2014). By collecting fresh saliva samples and culturing them on nutrient agar, individual colonies can be isolated. These colonies are preliminarily, identified through morphological observation, Gram staining, and basic biochemical testing such as the catalase and oxidase tests (Rods, 2014) (Shields & Cathcart, 2010).). This approach enables the selection of viable and representative bacterial strains reflecting the complexity of the oral microbiota. The isolates obtained through this procedure serve as a biological model for assessing how the material interacts with oral bacteria under controlled laboratory conditions.

8.2 Procedure :

Saliva samples were collected in sterile conditions by asking the subjects to refrain from eating or brushing their teeth for at least one hour before sampling. Each subject was instructed to spit directly into a sterile container (such as a sterile cup or Falcon tube) until approximately 1 to 2 mL of saliva was obtained. The saliva was gently homogenized, and a volume of 0.1 mL was extracted, either with a pipette or a sterile platinum loop, and streaked in striae on the surface of nutrient agar plates (GN). The inoculated plates were incubated at 37 °C for 24 to 48 hours to allow bacterial colonies to grow.

Following incubation, the colonies were observed, based on morphological characteristics such as size, shape, color, and texture. Representative colonies were then, subjected to Gram staining. A small drop of distilled water was placed on a clean microscope slide, and a single colony was picked using a sterile loop and spread to form a thin, circular smear. After air drying, the slide was heat-fixed by passing it briefly through a flame with the smear side facing up. The fixed smear was covered with crystal violet for one minute. After that, it was rinsed with distilled water. Then it was covered with Lugol’s iodine for another minute. After a second rinse, ethanol was applied dropwise for 10 seconds to decolorize, followed immediately by rinsing with distilled water. The slide was then, counterstained with fuchsine or safranin for one minute, rinsed again, and gently dried using a filter paper or by air. The slide was examined under an optical microscope using an oil immersion lens (100× objective).

To further identify, the bacteria, biochemical tests were carried out.

8.2.1 Oxidase test :

For the oxidase test, a fresh colony (24 h) was picked and rubbed onto an oxidase test disk or a piece of filter paper impregnated with tetramethyl-p-phenylenediamine reagent. A positive reaction was indicated by a visible color change.

8.2.2 Catalase test :

For the catalase test, a clean, dry glass slide was used to place a drop of 3 % hydrogen peroxide (H_2O_2), onto which a fresh colony was transferred using a sterile loop. The immediate appearance of oxygen bubbles indicated a positive result due to catalase activity.

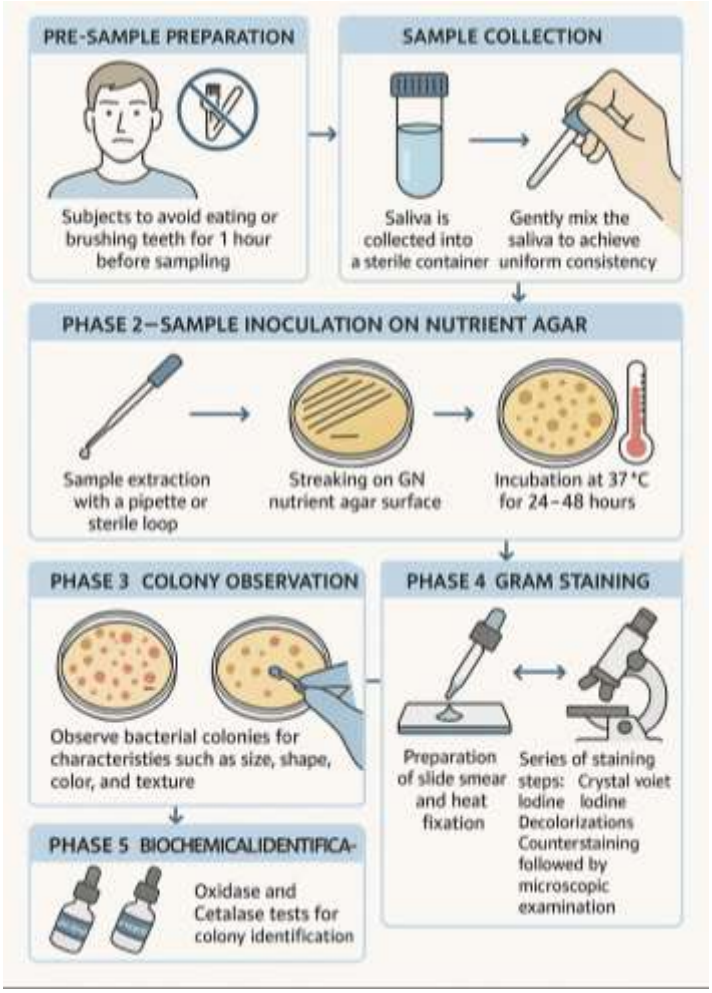

Figure IV-9 : Diagram of Microbiological Protocol

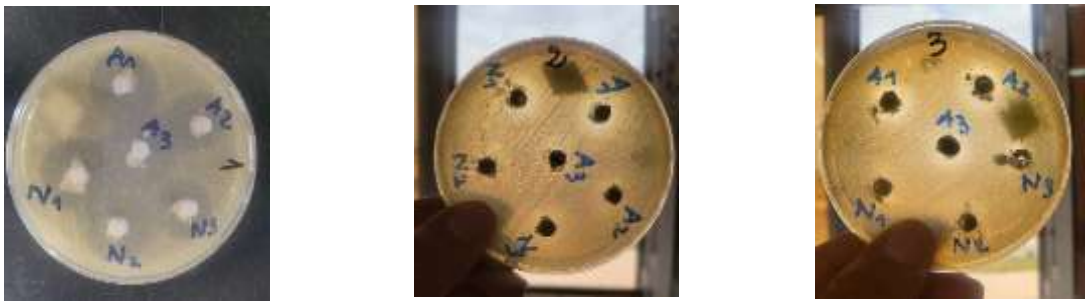

Petri dish showing inhibition zones produced against S. aureus souche 1

Petri dish showing inhibition zones produced against S. mutans Souche 2

Petri dish showing inhibition zones produced against E. coli Souche 3

Figure IV-10 : Zone of Inhibition Test Results

9. Antibacterial Properties of Zinc-Doped Hydroxyapatite Synthetic Dental Materials

Two series of Zn-doped hydroxyapatite (Zn–HAp) samples were synthesized using different Zinc precursors: Zinc nitrate $Zn(NO_3)_2$ and Zinc acetate $Zn(OOCCH_3)_2$. The samples prepared with Zinc nitrate are denoted ZnN–HAp, while those prepared with Zinc acetate are referred to as ZnA–Hap.

The antibacterial activity of Zn-Hap materials with different size (ZnA-75Hap, ZnA-106Hap, ZnA-45Hap) was compared with that of (ZnN-106Hap, ZnN-45Hap, ZnN-75Hap) in order to evaluate the combined effects of the zinc precursor type and the particle size of the calcium source on the material's biological activity."

9.1 Zone of Inhibition Measurements :

Using the Mueller–Hinton agar diffusion assay (per the provided protocol), we measured inhibition zones of each material against three oral bacterial strains. The results are shown in table IV-1 (zone diameters in millimeters):

In the table above, Smaller zones indicate weaker antibacterial activity (hence better compatibility with the oral flora).

Material ZnA-45Hap consistently shows the smallest inhibition zones for two of the strains and has the lowest combined total (41 mm) and average (~13.7 mm). In contrast, ZnA-75Hap and ZnA-106Hap have the largest totals (48–49 mm), implying stronger antibacterial effects. The samples prepared with Zinc nitrate fall in between. Overall, ZnA-45Hap produced the least bacterial inhibition in our tests.

Table IV-1 : inhibition zones of each material against three oral bacterial strains

Material	Souche 1 (mm)	Souche 2 (mm)	Souche 3 (mm)	Total (mm)	Average (mm)
ZnA-75Hap	22	13	13	48	16.0
ZnA-106Hap	20	15	14	49	16.3
ZnA-45Hap	20	9	12	41	13.7
ZnN-106Hap	25	12	8	45	15.0
ZnN-45Hap	22	14	10	46	15.3
ZnN-75Hap	20	14	10	44	14.7

In the synthesis of zinc-doped hydroxyapatite (Zn-HA) for antibacterial biomaterial applications, the choice of zinc precursor significantly influences nanoparticle morphology, ion-release behaviour and ultimately antibacterial efficacy. Using zinc acetate as the precursor confers several advantages: the acetate anion decomposes under milder conditions, facilitating homogeneous incorporation of Zn^{2+} into the HA lattice and promoting formation of smaller, well-dispersed crystallites with high specific surface area. This in turn enhances the availability of Zn^{2+} active sites at the particle surface and augments ion release into the surrounding medium, which is central to the antibacterial mechanism (membrane disruption, reactive oxygen species formation, enzyme inhibition) (Gatou, Lagopati, Vagena, Gazouli, & Pavlatou, 2022). In contrast, zinc nitrate precursors are prone to rapid decomposition, gas evolution (NO_x) and less controlled precipitation, which can lead to larger particle sizes, agglomeration and heterogeneous Zn distribution — thereby reducing effective surface exposure, lowering ion-release rates and producing weaker inhibition zones in microbial assays (Lehraki, et al., 2020). Accordingly, Zn-HA produced from zinc acetate precursors demonstrates greater and more consistent antibacterial performance, making it the preferred choice for antibacterial HA-based biomaterials.

9.2 Identification of the Most Biocompatible Material :

By the criterion of minimal inhibition, Material ZnA-45Hap emerges as the most biocompatible (least antibacterial) of the six. Its unusually low zones (especially the 9 mm zone on Souche 2 and 12 mm on Souche 3) suggest it has minimal effect on the tested bacteria. All other materials yielded substantially larger zones (up to 25 mm), indicating higher antibacterial potency and thus less compatibility with beneficial flora. For example, ZnA-106Hap's zones were 20–15–14 mm and total 49 mm, clearly higher than ZnA-45Hap's values.

These observations are consistent with known behavior of dental polymers. It is well documented that unmodified resin adhesives and composites typically exhibit negligible

antibacterial activity (Imazato, 2003) (Imazato, Kuramoto, Kaneko, Ebisu, & Russell, 2002) Chen et al. (2012). In practical terms, a material like ZnA-45Hap likely contains no active biocidal agents, so it does not significantly inhibit bacterial growth, which matches our small zones.

Conversely, materials incorporating antibacterial agents such as silver nanoparticles (Hashem, Ghobashy, & Abdel Hamid, 2022), quaternary ammonium monomers (Featherstone, 2022), or chlorhexidine (Gonçalves, et al., 2025) typically produce significantly larger inhibition zones. For instance, adding about 0.05–1% nano-silver to a resin matrix is known to significantly reduce bacterial growth and to significantly reduce biofilm viability when incorporated into adhesives. If any of the tested materials (particularly among the Zinc nitrate $Zn(NO_3)_2$ precursors group or Zinc acetate $Zn(OOCCH_3)_2$ precursors group.) included such agents, they would be expected to show the larger zones we observed. The absence of such additives in ZnA-45Hap explains its low antibacterial effect.

9.3 Comparison with Literature on Biocompatibility :

The goal of an "anti-caries" dental material is to inhibit pathogens without disrupting beneficial microbes. Reviews emphasize finding a balance between antibacterial strength and biocompatibility (Zhu, et al., 2022)

In our case, ZnA-45Hap's minimal zones suggest it best preserves the native oral flora while providing the necessary mechanical support. This aligns with recommendations that inert or unfilled resins (which lack leachable antimicrobials) be used when broad antimicrobial activity is not desired (Chen, , Suh, & Yang , 2018)

9. Conclusion :

Material ZnA-45Hap shows the least antibacterial activity in our zone-of-inhibition assay. This makes it the most biocompatible with beneficial oral bacteria, according to the data. Literature on dental biomaterials supports this interpretation: materials without built-in antimicrobials (or only low-pH acidity) produce very small or no inhibition zones whereas materials engineered with antibacterial fillers (like silver or zinc oxide) produce large zones (Reda & Park, 2024). Thus, our finding that ZnA-45Hap is least inhibitory is consistent with existing evidence that the absence of antimicrobial additives yields minimal bacterial killing.

References :

Bandyopadhyay, A., Mitra, I., Goodman, S. B., Kumar, M., & Bose, S. (2023). Improving biocompatibility for next generation of metallic implants. *Progress in Materials Science, 133*, 101053.

Chen, L., Suh, B. I., & Yang, J. (2018). Antibacterial dental restorative materials: A review. *American Journal of Dentistry, 31*(Special Issue B), 6B–12B.

Featherstone, J. D. (2022). Dental restorative materials containing quaternary ammonium compounds have sustained antibacterial action. *Journal of the American Dental Association, 153*(12), 1114–1120.

Fleet, M. E., Liu, X., & King, P. L. (2004). Accommodation of the carbonate ion in apatite: An FTIR and X-ray structure study of crystals synthesized at 2–4 GPa. *American Mineralogist, 89*(10), 1422–1432.

Gatou, M. A., Lagopati, N., Vagena, I. A., Gazouli, M., & Pavlatou, E. A. (2022). ZnO nanoparticles from different precursors and their photocatalytic potential for biomedical use. *Nanomaterials, 13*(1), 122.

Gonçalves, F., Silva, L. S., Roschel, J. N., de Souza, G. G., Campos, L. D., Varca, G. H., … Boaro, L. (2025). Antibacterial resin composites with sustained chlorhexidine release: One-year in vitro study. *Pharmaceutics, 17*(9), 1144.

Gopi, D., Indira, J., Kavitha, L., Sekar, M., & Mudali, U. K. (2012). Synthesis of hydroxyapatite nanoparticles by a novel ultrasonic-assisted mixed hollow sphere template method. *Spectrochimica Acta Part A: Molecular and Biomolecular Spectroscopy, 93*, 131–134.

Guo, B., Zhao, T., Sha, F., Zhang, F., Li, Q., Zhao, J., & Zhang, J. (2017). Synthesis of vaterite $CaCO_3$ microspheres by carbide slag and a novel CO_2-storage material. *Journal of CO_2 Utilization, 18*, 23–29.

Hashem, R., Ghobashy, S., & Abdel Hamid, Z. (2022). The efficacy of nanosilver-coated stainless steel brackets in prevention of enamel demineralization in orthodontic patients. *Al-Azhar Journal of Dental Science, 25*(4), 495–504.

Hossain, M. S., Mahmud, M., Sultana, S., Bin Mobarak, M., Islam, M. S., & Ahmed, S. (2021). Coupled effect of particle size of the source materials and calcination temperature on the direct synthesis of hydroxyapatite. *Royal Society Open Science, 8*(9), 210684.

Imazato, S. (2003). Antibacterial properties of resin composites and dentin bonding systems. *Dental Materials, 19*(6), 449–457.

Imazato, S., Kuramoto, A., Kaneko, T., Ebisu, S., & Russell, R. R. (2002). Comparison of antibacterial activity of simplified adhesive systems. *American Journal of Dentistry, 15*(6), 356–360.

ISO. (2000). *ISO 13779-2: Implants for surgery—Hydroxyapatite—Part 2: Coatings of hydroxyapatite*. London, UK: British Standards Institution.

Kothari, M., Hassan, A. A., Sahle-Demessie, E., El-Dieb, A., El-Hassan, H., & Al-Anazi, A. (2024). Sustainable synthesis of carbide slag waste-derived hydroxyapatite and its application for cationic dye adsorption. *Journal of Water Process Engineering*.

Lehraki, N., Attaf, A., Aida, M. S., Attaf, N., Othmane, M., & Bouaichi, F. (2020). Effect of different zinc precursors on structural and optical properties of ZnO thin films. *arXiv preprint* arXiv:2003.08487.

Li, M. O., Xiao, X., Liu, R., Chen, C., & Huang, L. (2008). Structural characterization of zinc-substituted hydroxyapatite prepared by hydrothermal method. *Journal of Materials Science: Materials in Medicine, 19*(2), 797–803.

Mao, S., Liu, Y., Zhang, T. A., & Li, X. (2020). Nano-$CaCO_3$ synthesis by jet-reactor from calcium carbide slag. *Materials Research Express, 7*(11), 115003.

Michael, F. M., Khalid, M., Ratnam, C. T., Chee, C. Y., Rashmi, W., & Hoque, M. E. (2016). Sono-synthesis of nanohydroxyapatite: Effects of process parameters. *Ceramics International, 42*(5), 6263–6272.

Popa, C. L., Deniaud, A., Michaud-Soret, I., Guégan, R., Motelica-Heino, M., & Predoi, D. (2016). Structural and biological assessment of zinc-doped hydroxyapatite nanoparticles. *Journal of Nanomaterials, 2016*, 1062878.

Rajesh, R., Hariharasubramanian, A., & Ravichandra, Y. D. (2012). Chicken bone as a bioresource for the bioceramic (hydroxyapatite). *Phosphorus, Sulfur, and Silicon and the Related Elements, 187*(8), 914–925.

Reda, A. T., & Park, J. Y. (2024). Zinc oxide-based nanomaterials for microbiostatic activities: A review. *Journal of Functional Biomaterials, 15*(4), 103.

Ren, F., Xin, R., Ge, X., & Leng, Y. (2009). Characterization and structural analysis of zinc-substituted hydroxyapatites. *Acta Biomaterialia, 5*(8), 3141–3149.

Rodríguez-Lugo, V., Karthik, T. V., Mandoza-Anaya, D., Rubio-Rosas, E., Villaseñor Cerón, L. S., Reyes-Valderrama, M. I., & Salinas-Rodríguez, E. (2018). Wet chemical synthesis of nanocrystalline hydroxyapatite flakes: Effect of pH and sintering temperature on structural and morphological properties. *Royal Society Open Science, 5*(8), 18096.

Rods, G. P. (2014). *UK standards for microbiology investigations*. Public Health England.

Senthilkumar, S., Dhivya, V., Sathya, M., & Rajendran, A. (2021). RETRACTED ARTICLE: Synthesis and characterization of magnetite/hydroxyapatite nanoparticles for biomedical applications. *Journal of Experimental Nanoscience, 16*(1), 159–179.

Shields, P., & Cathcart, L. (2010). Oxidase test protocol. *American Society for Microbiology*, 4, 1–9.

Troeltzsch, M., Pache, C., Probst, F. A., Troeltzsch, M., Ehrenfeld, M., & Otto, S. (2014). Antibiotic concentrations in saliva: A systematic review of the literature, with clinical

implications for the treatment of sialadenitis. *Journal of Oral and Maxillofacial Surgery, 72*(1), 67–75.

Zhu, J., Chu, W., Luo, J., Yang, J., He, L., & Li, J. (2022). Dental materials for oral microbiota dysbiosis: An update. *Frontiers in Cellular and Infection Microbiology, 12*, 900918.

General Conclusion

General Conclusion

The present study investigates the utilization of novel biomaterials with enhanced properties for application in dental ceramic coatings. The primary objective is to develop and characterize the microstructure and bioactivity of hydroxyapatite coatings synthesized via a wet-chemical precipitation method using carbide lime as a calcium precursor, followed by mechanochemical zinc doping, with the aim of optimizing microstructure, bioactivity, and antibacterial performance for oral applications.Various hydroxyapatite morphologies were achieved using carbide lime, a byproduct of linde gas production. Several key insights regarding the characteristics of the carbide lime feedstock are discussed and summarized, providing a comprehensive understanding of its influence on the resulting hydroxyapatite structures.

This study demonstrates the feasibility of transforming carbide lime, a by-product from the acetylene production unit at Linde Gas, Sidi Bel Abbès, into a sustainable calcium source for the synthesis of zinc-doped hydroxyapatite (Zn-HAp). Physicochemical characterization showed that the waste is mainly composed of $Ca(OH)_2$, with high alkalinity (pH ≈ 11.5), porosity (~77.5%), low bulk density (~0.83 $g \cdot cm^{-3}$), and a CaO content of ~65.7%, confirming its high reactivity for hydroxyapatite formation.

Hydroxyapatite was synthesized via a wet-chemical precipitation route. Various particle size fractions of the precursor carbide lime powder were employed to investigate the influence of the initial particle size on the structural and morphological properties of the obtained hydroxyapatite. The HA synthesized from smaller particle-sized starting materials (45–75 µm) exhibited a lower degree of crystallinity, whereas the samples prepared from larger particles (106 µm-HA) showed comparatively higher crystallinity. Structural analyses by XRD and FTIR confirmed the formation of the hydroxyapatite phase with characteristic phosphate and hydroxyl bands, while minor carbonate traces reflected partial carbonation of the precursor.

The synthesized HA powders were subsequently used as precursors for zinc doping, and Zn-HA powders were successfully obtained through the mechanochemical route. The incorporation of zinc, particularly using the acetate precursor, led to smaller particle sizes and enhanced antibacterial activity compared to nitrate-based doping routes. The synthesized Zn-HAp samples exhibited measurable antibacterial effects, with inhibition zones ranging from 9 to 25 mm, depending on zinc content and bacterial strain, while ZnA-45Hap showed the most balanced antibacterial response (≈13.7 mm), suggesting good compatibility with oral applications.

General Conclusion

These results validate the technical feasibility and scientific relevance of using local industrial waste to produce bioactive and antimicrobial ceramic materials. This research not only contributes to the development of sustainable processes in materials engineering, but also provides the scientific foundation for a future startup initiative aimed at producing locally engineered dental coatings based on zinc-doped hydroxyapatite, supporting Algeria’s efforts toward industrial autonomy and circular economy in the biomedical materials sector